Physically Motivated Quintessence

A thesis submitted in partial fulfillment of the requirement
for the degree of Bachelor of Science with Honors in
Physics from the College of William and Mary in Virginia

Ian J. Swanson

Nuclear and Particle Theory Group, Physics Department,
College of William and Mary, Williamsburg, VA 23187-8795

Accepted for ______________________
(Honors, High Honors, or Highest Honors)

____
Advisor: Marc Sher, Physics, W&M

____
Christopher D. Carone, Physics, W&M

____
Carl E. Carlson, Physics, W&M

____
Gina Hoatson, Physics, W&M

____
Carey K. Bagdassarian, Chemistry, W&M

Williamsburg, Virginia
May 2000

Contents

Physically Motivated Quintessence

Ian J. Swanson

Abstract

Tracking quintessence models are arguably the most promising class of post-inflationary cosmological models, presenting simultaneous solutions to the cosmological coincidence and fine-tuning questions that have weakened other approaches to the missing energy problem. Cosmologists are still charged with the task of presenting a well motivated particle physics model of tracking quintessence in which the low mass fields associated with these solutions arise naturally. In this thesis I present a quintessence model generated by two independent seesaw models of neutrino masses. The neutrino mass mixing parameter Δm^2 determines the energy scales in the different sectors of this model. Tracking behavior is exhibited for a range of initial field values that spans nearly 30 orders of magnitude. By imposing theoretical and observational constraints, it is determined that the present model allows best-fit equation of state solutions ($-0.72 \leq w_Q \leq -0.58$) [7] for small-angle flavor mixing in the MSW plane. Centroid values of large-angle mixing solutions are excluded from the best-fit regions of parameter space. The model presented in this thesis is a physically motivated and cosmologically viable model of tracking quintessence.

The existence of zero-point energy fluctuations in QED are a central concept in any physical model dependent upon the energy density of the vacuum. As an appendix,[1] I include a brief study of zero-point QED vacuum fluctuations in the context of Schwinger's dynamical Casimir effect. Working from calculations describing a terrestrial analogue, I show that rapid dielectric changes in the QED vacuum generate intense energy bursts on astrophysical scales. Fluences generated by this mechanism may explain gamma-ray bursts.

[1] This appendix was completed outside of the Honors Research course Physics 495/496.

1 Introduction

The Cold Dark Matter (CDM) paradigm has dominated theoretical cosmology for decades. While black holes, planets and asteroids contribute to the dark matter fraction of the universe, hypothetical particle species such as Weakly Interacting Massive Particles (WIMPs), supersymmetric particles, and Massive Compact Halo Objects (MACHOs) are more important to cosmological history. CDM refers to dark matter particles that are non-relativistic. Perturbations in CDM species therefore evolve differently than their relativistic, or Hot Dark Matter (HDM), counterparts. Standard CDM (SCDM), CDM models employing a cosmological constant (ΛCDM), and CDM plus hot dark matter (HCDM), share a common foundation, within which quantum fluctuations in one or more inflationary fields are imprinted on early distributions of dark matter particles. Adiabatic perturbations in primordial matter distributions grow by gravitational instability, giving rise to structure formation and leaving behind a fossil record of the early universe in the Cosmic Microwave Background (CMB). Several recent observations favor models in which the ratio of the dark plus baryonic matter density to the critical density (Ω_m) is roughly 1:3 [1]. A Hot Dark Matter (HDM) component generally contributes to structure on small scales [2, 3]. It is generally agreed that large scale structure is affected primarily by the presence of CDM, and the HDM fraction in the universe is minimal ($\Omega_{HDM} \ll \Omega_{CDM}$).

The shortcomings of both SCDM and ΛCDM models arise on theoretical and observational platforms. Theoretically, cosmologists prefer flatness in the context of an inflationary universe. The success of inflation [4, 5, 6] is due largely to its solution to the cosmological horizon and flatness problem and its prediction of scale-invariant energy density fluctuations [7]. For these and other reasons, theorists have adopted variants of the inflationary model as cosmological principle and, in turn, have assumed a geometrically flat universe. Using $H_0 = 65 \pm 10$ km s^{-1} Mpc^{1} [8, 9], the most successful cosmological models indicate [7, 1, 10, 11]

$$\begin{aligned}\Omega_m &\equiv [\Omega_{CDM}] + [\Omega_{Baryon}] \\ &\approx [0.30 \pm 0.10] + [0.04 \pm 0.01].\end{aligned}$$

Consequently, SCDM models are forced to abandon the flat metric implied by inflation, or assume some missing energy component Ω_E such that the total density fraction coincides with the inflationary picture ($\Omega_0 = 1$).

Measurements of mass power spectra [1, 13, 14] and luminosity-redshift relationships in type Ia supernovae [15] also indicate an additional energy component with negative pressure and equation of state. In natural units, observations indicate $\rho_{\text{vac}} \approx 10^{-48}$ GeV^4. An additional energy contribution is also required to reconcile the estimated age of the universe with the observed value of Hubble's constant H_0. Several methods, including observations of globular clusters, allow approximations of the current age of the universe: $t_0 \approx 13 - 15$ Gyr [17]. In the standard FRW cosmology, values of Ω_E required to combine age estimates with estimates of H_0 are consistent with $\rho_{\text{vac}} \approx \mathcal{O}(\text{meV}^4)$.

Historically, the most common form of Ω_E has been the cosmological constant Λ, appearing as an integration constant in Einstein's field equations:

$$R_{\mu\nu} - \frac{1}{2} g_{\mu\nu} R - \Lambda g_{\mu\nu} = -8\pi G T_{\mu\nu}. \tag{1}$$

The equivalence of Λ and vacuum energy density can be seen by noting that $T_{\mu\nu}$, by Lorentz invariance, must take the form ($g_{00} = -1$)

$$\langle T_{\mu\nu} \rangle = -\langle \rho \rangle g_{\mu\nu}, \tag{2}$$

such that the effective cosmological constant is

$$\Lambda_{\text{eff}} = \Lambda + 8\pi G \langle \rho \rangle, \tag{3}$$

contributing a total vacuum energy ρ_{vac} of the form:

$$\rho_{\text{vac}} = \langle \rho \rangle + \frac{\Lambda}{8\pi G} = \frac{\Lambda_{\text{eff}}}{8\pi G}. \tag{4}$$

The cosmological constant Λ can therefore be characterized as a positive, spatially homogeneous contribution to the vacuum energy density of the universe with negative pressure.

Conceptual problems arise with the introduction of an arbitrary homogeneous energy density of the form (4) into the vacuum. To see this, one may estimate the order of magnitude of Λ. As it is currently understood, the early universe experiences several spontaneous symmetry breaking phase transitions after the Big Bang. A phase transition induced at temperature T gives rise to a shift in vacuum energy density associated with the Higgs field of order T^4. In the early universe, T takes values as high as the GUT scale. One may also attempt a direct calculation of ρ_{vac} by summing over the zero-point modes $\mathbf{k}$ of the quantum vacuum within a quantization volume V. Employing a quantum field theory that accounts for degrees of freedom at energies below $\approx$ 100 GeV, and assuming that radiative corrections appear only in adjustments of the effective Lagrangian, one may guess that, in natural units:

$$\rho_v = \frac{\Lambda}{8\pi} + \frac{1}{2} V \int \frac{d^3\mathbf{k}}{(2\pi)^3}\mathbf{k}, \tag{5}$$

indicating $\rho_v \approx (100 \text{ GeV})^4$. In the context of relevant energy scales in particle physics, the theoretically expected value of the vacuum energy density, or equivalently Λ, is roughly fifty-six orders of magnitude too large. When studying ΛCDM models, it is conventional to assume some undiscovered symmetry of nature or other mechanism that brings about the necessary cancellations to resolve this discrepancy.

The most decisive observational tests of CDM cosmologies are the power spectrum of primordial mass perturbations, and the anisotropy signature of the CMB. In general, SCDM models generate poor fits to the observed mass power spectrum. Furthermore, by matching large-scale SCDM predictions with COBE data, the amplitude of fluctuations in the CMB on 8 h^{-1} Mpc scales ($H_0 \equiv 100\mathrm{h}$ km s^{-1} Mpc^{-1}) is found to exclude the SCDM approach [16]. Although the shape of the mass power spectrum in ΛCDM models matches observation more closely than SCDM models, Wang *et al.* have shown that ΛCDM power spectra fail precision shape tests based on the Peacock APM survey data [7, 19]. Furthermore, the overall amplitude of ΛCDM power spectra as fixed by standard COBE normalization excludes these models, requiring antibiasing of galaxy distributions relative to corresponding mass autocorrelation functions [18].

To address the inability of SCDM and static ΛCDM models to generate mass perturbation spectra and CMB anisotropies that are corroborated by observation, many authors have considered the possibility of a time-varying cosmological constant [20, 21, 22, 23]. The central prospect behind this approach is that Λ was large at early epochs, underwent a slow decay due to some physical process, and presently contributes a vacuum energy $\rho_{\mathrm{vac}} = \mathcal{O}(\mathrm{meV}^4)$. Although this approach adjusts the COBE normalization of the mass power spectrum, dynamic Λ models are generally not able to support long-wavelength fluctuations and hence predict CMB anisotropies that are inconsistent with COBE data. The parameter Λ must also span tremendous energy scales, requiring extensive fine tuning scenarios (to 1 part in $\approx 10^{120}$ [12]) that are difficult to motivate physically, a problem known as *Cosmic Coincidence* [24]. Comprehensive analyses of perturbation spectra generated by decaying Λ also exclude these models [7].

The problematic characteristic of ΛCDM models is spatial homogeneity. In response to the inability of SCDM, HCDM and both static and dynamic ΛCDM models to generate observationally consistent cosmological histories, theorists have recently focused on the possibility that Ω_E is generated by quintessence: a dynamic, spatially inhomogeneous form of vacuum energy. The most widely studied form of quintessence consists of slowly evolving scalar fields in the vacuum [25, 26, 27, 28, 29]. Quintessence occurs when a field ϕ evolves slowly down a potential, giving rise to a small vacuum energy with negative pressure. This class of models, combined with cold dark matter, is known collectively as QCDM. All such solutions require some sort of slowly evolving or oscillating field at the present epoch, providing kinetic energy densities less than the corresponding potential energy densities. Quintessence naturally supports long-wavelength fluctuations while maintaining nearly scale-invariant energy density and flatness. Slow evolution is required to provide negative pressure. For a scalar field ϕ evolving in a positively-valued potential $V(\phi)$, the energy density and pressure contributions are $\rho = (1/2)\dot{\phi} + V(\phi)$; $p = (1/2)\dot{\phi} - V(\phi)$, respectively. The COBE normalization of the power spectrum is set by the pressure contribution, allowing a parameterization of both the normalized amplitude and the relative contributions at all scales. The equation of state, defined by $w_Q \equiv p/\rho$, is characterized in quintessence models by $w_Q \in (-1, 0]$. For a given set of fixed cosmological parameters, quintessence generally provides smaller acceleration at late epochs. Conceptually, quintessence is distinguished from spatially homogeneous dynamic Λ models by its inhomogeneous, dynamic contribution to the vacuum energy and pressure.

Although quintessence models are apparently successful in accommodating observational constraints, solutions are still faced with the problem of cosmological coincidence and fine-tuning. Both dynamic Λ and QCDM models must explain why the present value of the vacuum energy density is comparable with the matter density, and why this energy component is small compared to relevant scales in particle physics. These problems are addressed in the context of quintessence scenarios by the use of tracker fields. Tracking quintessence models exhibit attractor-like solutions on cosmological time scales, providing observationally desirable cosmological histories that are insensitive to initial conditions over roughly 100 orders of magnitude [12, 30, 33]. Tracking solutions alleviate the problem of coincidence and fine-tuning, while accommodating physically motivated initial conditions such as post-inflationary equipartition. The quintessence equation of state w_Q in tracking models may or may not follow the background equation of state w_B. Observationally consistent QCDM models, however, exhibit w_Q that approaches w_B at late epochs, eventually dominates, and drives an accelerated expansion observed in the present epoch [30].

Tracking quintessence CDM models compensate for a wide degree of theoretical and observational constraints, and are perhaps at present the most promising class of post-inflationary cosmological models. The question of small energy scales, however, is left to the logical introduction of ultra low-mass fields. Several authors have explored the implications of quintessence in supersymmetry. Another approach employs the mass hierarchy seen in the physics of neutrino flavor mixing via the MSW mechanism. In 1995, A. Singh [34] presented a theory of Late-Time Phase Transitions (LTPTs) based on the seesaw mechanism [35] of generating small energy scales in the neutrino mass matrix. We observe that Singh's model, based solely on SU(2) $(\nu_e - \nu_\mu)$ mixing, generates a quintessence cosmology with pseudo-tracking solutions. Although Singh's approach produces observationally consistent acceleration in the present epoch, the model, as presented by Singh, generates invalid cosmological histories. We show that observational constraints are met with the introduction of an independent but similar $(\nu_\mu - \nu_\tau)$ seesaw mechanism.

In section 2.2 I review the physical model presented by Singh, augmenting the Yukawa couplings to include a $(\nu_\mu - \nu_\tau)$ seesaw mechanism in the leptonic sector.

Quintessence cosmology and tracking solutions are reviewed in section 2.3. In section 2.4, employing the parameterization convention for quintessence cosmological models developed by Wang, Caldwell, Ostriker and Steinhardt [7], I compare cosmological properties of the augmented seesaw model against best-fit restrictions on the parameter space.

2 Physical models

In reference [34], Singh constructed a two family (ν_e – ν_μ) SU(2) seesaw mechanism. For completeness, I restate the essential physics of this mechanism.

Two right-handed neutrinos N_R^i transform as the fundamental representation of a global $\mathrm{SU_R}(2)$ symmetry, implemented in the right-handed Majorana mass term by the introduction of the Higgs field σ_{ij}. When the Higgs field acquires its vacuum expectation value (VEV) $\langle\sigma\rangle$, $\mathrm{SU_R}(2)$ is broken to U(1), creating two Pseudo-Nambu-Goldstone Bosons (PNGBs). This symmetry breaking generates right-handed Majorana masses M associated with the GUT scale. When the neutrino mass matrix is diagonalized, the mass eigenvalues are suppressed by $1/M$. Nambu-Goldstone (NG) modes arise through fermion loop corrections when $\mathrm{SU_R}(2)$ is broken in the Dirac sector, as the lepton doublets l_L and Higgs doublet Φ are singlets in this symmetry.

The neutrinos couple to the Higgs field according to

$$-\mathcal{L} = y_{ai}\bar{l}_L^a N_R^i \Phi + y\bar{N}_R^i N_R^{j\ c}\sigma_{ij} + H.C., \tag{6}$$

with $a, i, j, = 1, 2$. Assuming the Higgs field σ acquires a VEV of the form $\langle\sigma_{ij}\rangle = f\delta_{ij}$, $\sigma(x)$ may be parameterized in terms of $\mathrm{SU_R}(2)$ matrices $U(x)$ according to

$$\begin{aligned} \sigma(x) &= U(x)\langle\sigma\rangle U^T(x) && (7)\\ &= fU(x)U^T(x); && (8)\\ U(x) &\equiv \exp[i(\phi_1\tau_1 + \phi_2\tau_3)/f], && (9) \end{aligned}$$

where τ_i are the Pauli matrices. To one loop, the renormalized effective potential for the background fields ϕ_i is

$$V_r = V_0 + m^2\mathcal{M}^2 + \lambda_r(\mathcal{M}^2)^2 - \frac{(\mathcal{M}^2)^2}{8\pi^2}\left(\ln\frac{\mathcal{M}^2}{\mu^2} - \frac{1}{2}\right), \tag{10}$$

The quantity $\mathcal{M}^2$ takes the form

$$\mathcal{M}^2 = \frac{(m^2)^2}{M^2}(\cos^2 2||\phi|| + \hat{\phi}_2 \sin^2 2||\phi||), \tag{11}$$

with the field magnitude and norm defined by:

$$||\phi|| \equiv \sqrt{\phi_1^2+\phi_2^2}/f \tag{12}$$

$$\hat{\phi}_i \equiv \phi_i/\sqrt{\phi_1^2+\phi_2^2}. \tag{13}$$

The parameter μ is the usual renormalization scale. Mathematically, the effects of λ_r can be absorbed into to value of μ To connect with neutrino oscillation experiments, note that the physically observable mass parameter is the mixing mass term Δm^2. When the SU(2) symmetry is broken and the Higgs doublet Φ acquires its VEV, denoted by $\langle\Phi\rangle \equiv v$, the mass couplings for the neutrino fields become

$$-\mathcal{L} = m_{ai}\bar{\nu}_L^a N_R^i + M\bar{N}_R U U^T N_R^c + H.C. \tag{14}$$

The Majorana masses M are associated with the VEV of the Higgs singlet, $M = yf/\sqrt{2}$, while the mass matrices m_{ai} are associated with the VEV of the doublet. The VEV magnitude f is assumed to be much larger than the doublet magnitude v. One may estimate the induced form of σ in terms of the singlet VEV and m_ν [36], obtaining $\langle\sigma_{ij}\rangle < (10^{15})\delta_{ij}$ GeV, or $f < 10^{15}$ GeV. This constraint is consistent with conventional understandings of the seesaw mechanism [35, 37, 38]. To explicitly break the $\mathrm{SU_R}(2)$ symmetry of this model, the coupling strength of the neutrino fields to the ϕ_i fields, y_{ai}, should be nonzero. Setting $y_{ai} = 0$ enhances the symmetry of the Lagrangian, reducing the ability of the system to generate PNGB modes.

The time evolution of Singh's $(\nu_e - \nu_\mu)$ model appears in (Fig. 1). For $V_0 \approx m_\nu^4$, and $m \approx m_\nu$, the evolving fields ϕ_i generate a vacuum energy density ρ_ϕ in the present epoch that is consonant with observation. When Singh's model is evolved in the presence of the standard background cosmology, ρ_ϕ dominates at late epochs and generates an acceleration corresponding to $H_0 \approx 65$ km sec^{-1} Mpc^{-1}.

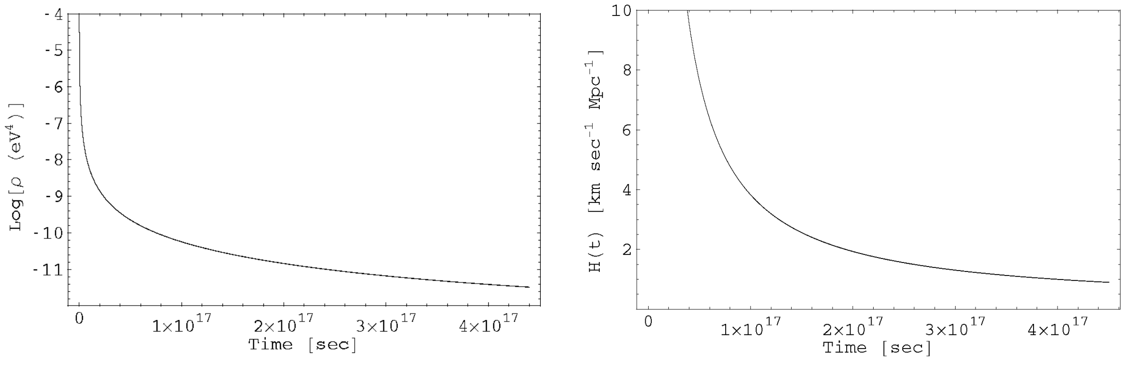

(a) (b)

Figure 1: $(\nu_e - \nu_\mu)$ quintessence in A. Singh's SU(2) seesaw model [34]. The energy density (a) contributed by the evolution of ϕ_i in V_r dominates in the present epoch and is characterized by $\rho_\phi \approx \mathcal{O}(\text{meV}^4)$. The behavior of the Hubble parameter due to ϕ_i quintessence (b) is given in units of 65 km sec^{-1} Mpc^{-1}, and is seen to approach $H_0 \approx 65$ km sec^{-1} Mpc^{-1} at late times.

The introduction of a similar but independent SU(2) $(\nu_\mu - \nu_\tau)$ seesaw model is straightforward. Adjustments to Singh's approach are obtained by adding couplings analogous to those appearing in eqn. (6) to the Lagrangian. The symmetry breaking mechanism of additional components are identical to that outlined above, though additional coupling strengths g_{ai} and g are included and new mass parameters are present associated with $(\nu_\mu - \nu_\tau)$ flavor mixing. As before, the Higgs field σ_{ij} is parameterized by exploiting the global SU(2) symmetry. For clarity, we denote the parameterization fields associated with $(\nu_\mu - \nu_\tau)$ mixing by ξ_1 and ξ_2, such that the SU(2) matrices appear as $U(x) = \exp[i(\xi_1\tau_1 + \xi_2\tau_3)/f]$ in the $(\nu_\mu - \nu_\tau)$ sector. While the additional seesaw model is nearly identical in structure to the original mechanism (6), the evolution of the ξ_i fields in the $(\nu_\mu) - \nu_\tau$ sector generate cosmological histories that are vastly different from those provided by the Singh model alone. The renormalized potential V_r in the new, or augmented Lagrangian is shown in Figure 2.

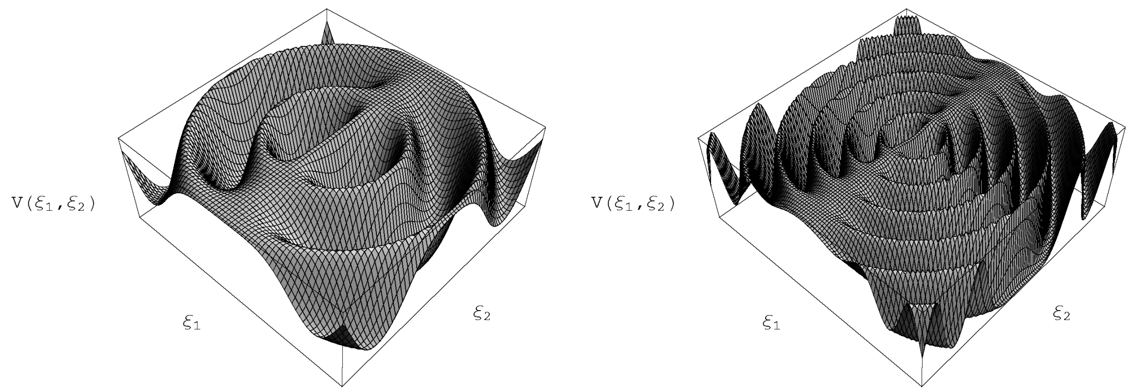

(a) (b)

Figure 2: Renormalized potential in the modified $(\nu_e - \nu_\mu) + (\nu_\mu - \nu_\tau)$ model. This potential V_r generates PNGB modes with the explicit breaking of $\mathrm{SU_R}(2)$ in the Dirac sector. The scale in (b) is enlarged by a factor of 2.2. The oscillation pattern repeats indefinitely moving outward from the origin.

Including a new energy scale in the Lagrangian by assuming separate couplings and mass parameters is an oversimplified approach. There cannot be four completely uncoupled right-handed neutrinos N_R^i. If couplings in the Dirac and Majorana terms take the generalized form:

$$\mathcal{L}_D = \left(\bar{\nu}_e \; \bar{\nu}_\mu \; \bar{\nu}_\tau \right) \begin{pmatrix} y_{11} & y_{12} & 0 & 0 \\ y_{21} & y_{22} & g_{22} & g_{23} \\ 0 & 0 & g_{32} & g_{33} \end{pmatrix} \begin{pmatrix} \nu_1 \\ \nu_2 \\ \nu_3 \\ \nu_4 \end{pmatrix} \qquad (15)$$

and

$$\mathcal{L}_M = f \begin{pmatrix} \bar{\nu}_1 & \bar{\nu}_2 & \bar{\nu}_3 & \bar{\nu}_4 \end{pmatrix} \begin{pmatrix} y & 0 & 0 & 0 \\ 0 & y & 0 & 0 \\ 0 & 0 & g & 0 \\ 0 & 0 & 0 & g \end{pmatrix} \begin{pmatrix} \nu_1 \\ \nu_2 \\ \nu_3 \\ \nu_4 \end{pmatrix}, \tag{16}$$

the couplings in the mass matrix appear as:

$$\frac{1}{f} \begin{pmatrix} \frac{y_{11}{}^2+y_{12}y_{21}}{y} & \frac{y_{11}y_{21}+y_{12}y_{22}}{y} & 0 \\ \frac{y_{21}(y_{11}+y_{22})}{y} & \frac{y_{21}{}^2 g+y_{22}{}^2 g+g_{22}{}^2 y+g_{23}{}^2 y}{yg} & \frac{g_{22}g_{32}+g_{23}g_{33}}{g} \\ 0 & \frac{g_{22}g_{32}+g_{23}g_{33}}{g} & \frac{g_{32}{}^2+g_{33}{}^2}{g} \end{pmatrix} \tag{17}$$

When mass eigenvalues are considered, there is a complex interdependence among the couplings associated with the various energy scales in the new Lagrangian. Fortunately, this interdependence does not place any serious restrictions on the viable parameter space in this model. In more tightly constrained models, the interdependence in (17) must be considered.

3 Quintessence cosmology: parameterization and constraints

In quintessence cosmology, the universe is characterized by spatial flatness and obeys the physics of the FRW metric throughout most of cosmological history. Late-time behavior is governed by the introduction of an evolving scalar field whose energy density tracks the background cosmology but remains subdominant until the present epoch. At late times, the quintessence component dominates, providing negative pressure and a spatially inhomogeneous energy density that is roughly comparable to ρ_{matter}.

In the standard FRW universe, dynamical evolution of the fields ϕ_i and ξ_i, (introduced through $\mathrm{SU_R}(2)$ symmetry in the seesaw mechanism of section 2), contribute an energy density and pressure to the vacuum [39]:

$$\rho_Q = \frac{\dot{\phi}_1^2 + \dot{\phi}_2^2}{2} + \frac{\dot{\xi}_1^2 + \dot{\xi}_2^2}{2} + V(\phi_1,\phi_2) + V(\xi_1,\xi_2) \tag{18}$$

$$p_Q = \frac{\dot{\phi}_1^2 + \dot{\phi}_2^2}{2} + \frac{\dot{\xi}_1^2 + \dot{\xi}_2^2}{2} - V(\phi_1,\phi_2) - V(\xi_1,\xi_2). \tag{19}$$

The time evolution of the scale factor $a(t)$ can be extracted from the equations of motion that govern $\xi_i(t)$ and $\phi_i(t)$ and Einstein's field equations (1):

$$0 = \ddot{\phi}_1 + \ddot{\xi}_1 + 3\frac{\dot{a}(t)}{a(t)}(\dot{\phi}_1 + \dot{\xi}_1) + \frac{\partial V}{\partial \phi_1} + \frac{\partial V}{\partial \xi_1}, \tag{20}$$

$$0 = \ddot{\phi}_2 + \ddot{\xi}_2 + 3\frac{\dot{a}(t)}{a(t)}(\dot{\phi}_2 + \dot{\xi}_2) + \frac{\partial V}{\partial \phi_2} + \frac{\partial V}{\partial \xi_2}. \tag{21}$$

Equations (20) and (21) can be solved numerically. If ξ_i or ϕ_i are oscillatory, the time-scale over which the energy contained in these fields decays into neutrinos is given by the decay-width formula (see, eg. [39])

$$\Gamma^{-1} \simeq f\frac{8\pi}{y^2 m_\nu^2}. \tag{22}$$

In this case, the equations of motion (20,21) acquire decay terms of the form:

$$0 = \ddot{\phi}_i + \ddot{\xi}_i + 3\frac{\dot{a}(t)}{a(t)}(\dot{\phi}_i + \dot{\xi}_i) + \frac{\partial V}{\partial \phi_i} + \frac{\partial V}{\partial \xi_i} + \Gamma_\phi \dot{\phi}_i + \Gamma_\xi \dot{\xi}_i. \tag{23}$$

In [7], Wang, Caldwell, Ostriker and Steinhardt reduced the parameterization of general quintessence models to five basic quantities: (i) the equation of state $w_Q \equiv p/\rho$, (ii) the matter fraction Ω_m, (iii) the baryon fraction Ω_b, (iv) the Hubble parameter $H(t)$, and (v) the index of the mass power spectrum n_s. These parameters were considered in the context of a wide class of observational constraints, including those associated with Big Bang nucleosynthesis, precision shape tests of the mass power spectrum, high-redshift type Ia supernovae observations, gravitational lensing counts, cluster evolution dynamics, COBE normalization techniques, and small-angle CMB anisotropies. Wang *et al.* were able to exclude a large region of parameter space based on these constraints, concluding that best-fit quintessence models generating observationally consistent cosmological histories are characterized by the following [7]:

$$
\begin{aligned}
w_Q &\approx -0.65 \pm 0.07, && (24)\\
\Omega_m &\approx 0.33 \pm 0.05, && (25)\\
\Omega_b &\approx 0.046 \pm 0.005, && (26)\\
H_0 &= 65 \pm 15 \text{ km s}^{-1} \text{ Mpc}^{-1}. && (27)
\end{aligned}
$$

While the best-fit equations of state satisfy (24), values within the range $-1 \leq w_Q \lesssim -0.2$ are consistent at the 2σ level with low redshift observations, CMB anisotropy signatures, and spectral and photometric measurements of type Ia supernovae [7]. Variations in the spectral index n_s control tensorial contributions to the mass power spectrum, and do not induce notable changes in the cosmological picture. For simplicity, we set $n_s = 1$. ΛCDM models, by comparison, have an equation of state that is precisely $w_Q = -1$ at all times.

Although the constraints studied in [7] were developed using quintessence models with constant equation of state w_Q, the use of an effective equation of state defined by [40]

$$w_{\text{effective}} \equiv \frac{\int da\Omega_Q(a)w_Q(a)}{\int da\Omega_Q(a)} \tag{28}$$

reproduces the fundamental physics of these models, allowing a direct comparison of dynamic QCDM models to the parameter constraints in eqns. (24 – 27). This expression is a weighted average of the instantaneous equation of state as a function of the scale factor a. The expression is normalized in the denominator by the integral over the weight, or the quintessence fraction Ω_Q. The augmented seesaw model in the present discussion exhibits a dynamical equation of state. Henceforth, the parameter w_Q, when used in reference to this model, will refer to the effective equation of state defined by (28).

Two facets of the so-called cosmological constant problem also arise in the discussion of quintessence cosmological models: (i) cosmological coincidence and (ii) fine-tuning. The problem of cosmological coincidence asks how an additional energy component, whose initial conditions may be arbitrary, automatically tracks the background cosmology for roughly 12 – 14 billion years, dominates only in the present epoch, and chooses a magnitude at late times comparable to the background matter density. The fine-tuning problem questions the smallness of the present energy density relative to most other energy scales in particle physics. While cosmological tracking solutions are designed to directly confront the coincidence problem, the augmented seesaw model in the present discussion deals more naturally with the question of fine-tuning.

Steinhardt, Wang and Zlatev have reduced the study of tracking solutions to a parameter-based analysis of the potential in which a scalar quintessence field evolves [30]. The existence of tracking solutions is determined by a quantity Γ defined for a quintessence potential $V(\xi_i)$ by:

$$\Gamma \equiv V(\xi_i)\frac{\partial^2 V(\xi_i)}{\partial \xi_i^2}\left(\frac{\partial V(\xi_i)}{\partial \xi_i}\right)^{-2}. \tag{29}$$

For quintessence models with effective equation of state less than that of the background cosmology, tracking behavior is exhibited in potentials for which $\Gamma > 1$ and

$$\left|\frac{d}{dt}\left(\frac{\Gamma - 1}{H}\right)\right| \ll |\Gamma - 1|. \tag{30}$$

Defining γ_Q as

$$\gamma_Q \equiv \left|\left(\frac{1}{V(\xi_i)}\frac{\partial V(\xi_i)}{\partial \xi_i}\right)\right|, \tag{31}$$

Steinhardt *et al.* [30] note that, for $w_Q < w_{\mathrm{Background}}$, tracking does not occur for increasing γ_Q over regions of decreasing $V(\xi_i)$. Quintessence models that exhibit an effective equation of state greater than the background equation of state do not generate viable cosmological models. The generalized analysis advanced in [30] allows quintessence potentials to be systematically tested for tracking behavior.

4 Cosmology with an augmented seesaw model

4.1 Basic properties

The study of quintessence and tracking cosmology has been rigorously parameterized and standardized for most models. The viability of Singh's original seesaw mechanism or of the augmented seesaw mechanism presented in section 2.2 can be studied in the context of the parameterization techniques developed in [7, 12, 30].

It is helpful to observe the basic cosmological properties of these models, beginning with the behavior of the scalar fields themselves as they evolve in their effective potentials V_r (Fig. 2). The ϕ_i fields in Singh's (ν_e – ν_μ) model are damped in this potential. After symmetry breaking, ϕ_i evolve slowly to their minima, oscillating only during late epochs (see Fig. 3, (a)). It is precisely this slow kinetic evolution that generates negative pressure observed in the present epoch. The ξ_i fields in the (ν_μ – ν_τ) sector of the augmented (ν_e – ν_μ) + (ν_μ – ν_τ) model are underdamped, and oscillate rapidly about the minima of V_r until these oscillations decay into particles (see Fig. 3, (b)). These ξ_i oscillations begin early, roughly 1.6×10^{11} sec after the Big Bang. The frequency of ξ_i oscillations is greater than $\mathcal{O}(10^{10}$ Hz) when the fields first cross the minima of V_r. The frequency and amplitude rapidly decrease after $t \approx 1.6 \times 10^{11}$ sec, becoming microscopic at late times (see Fig. 3, (c)). Although the oscillation period of ξ_i grows rapidly after $t \approx 1.8 \times 10^{11}$ sec, the mass mixing parameter oscillates only at early epochs (Fig. 3, (d)), stabilizing at $t \approx 2 \times 10^{10}$ sec and never exiting the Δm^2 99% (CL) allowed region for (ν_μ – ν_τ) mixing indicated by the Super Kamiokande neutrino experiment [31] (see Fig. 11 below).

The physical contribution of the (ν_μ – ν_τ) sector to the quintessence energy density is driven solely by the rapid evolution of ξ_i fields to their minima in V_r before subsequent oscillation and decay into particles. The free parameters in the (ν_μ – ν_τ)

sector are the coupling strength g and the mass scale Δm^2 in eqn. (11). Explorations of the changes in this parameter allowed by empirical results [31], and of arbitrary changes in the coupling strength g, indicate that the cosmological history of the $(\nu_e - \nu_\mu) + (\nu_\mu - \nu_\tau)$ model is largely insensitive to physical variations in these quantities. The $(\nu_\mu - \nu_\tau)$ sector is "turned on" for coupling strengths $g \sim \mathcal{O}(10^{-6})$ and larger. As g is increased above $\mathcal{O}(10^{-6})$, the cosmological history is invariant until the energy density contained in ξ_i approaches the background radiation density, causing exponential expansion and observationally untenable cosmological consequences. Thus, for physically reasonable values of the coupling strength, and empirically allowable values of the mass scale, the resulting cosmology in the augmented model is independent of fine-tuning[2] within the $(\nu_\mu - \nu_\tau)$ sector.

The overall contribution to the vacuum energy density from the augmented system can be extracted from the background cosmology and compared with the standard FRW forms of matter and radiation density (see Fig. 4). The free parameters that affect the late-time behavior of the system are the coupling strength y and the mass parameter Δm^2 associated with $(\nu_e - \nu_\mu)$ mixing. The behavior of ρ_ν at early times is determined primarily by the choice of initial conditions. In Figure 4, I choose to study a quintessence scenario in which the energy density generated by the neutrino fields does not track to the background cosmology until late times. These scenarios are interesting; they are guaranteed to preserve the FRW cosmology until the present epoch, and are generally more difficult to generate in the context of generic quintessence scenarios. For $t \lesssim 10^{10}$ sec, the energy density contribution of the augmented system, denoted by ρ_ν, is much less than the background matter and radiation densities. After $t \approx 10^{10}$ sec, ρ_ν begins to track the background cosmology. This tracking behavior continues until ρ_ν dominates at late times (see Fig. 4, (a)). The effect of varying the

[2]Not to be confused with the so-called *fine-tuning problem* discussed in section 2.3.

mixing parameter Δm^2 in the $(\nu_e - \nu_\mu)$ sector is significant for $t \sim \mathcal{O}(10^{17}$ sec) and greater. Increasing this mass parameter raises the final dominant value of ρ_ν. Note that ρ_ν does not dominate in the present epoch unless $\Delta m^2 \sim 6.3 \times 10^{-6}$ eV^2 or greater (see Fig. 4 (b)).

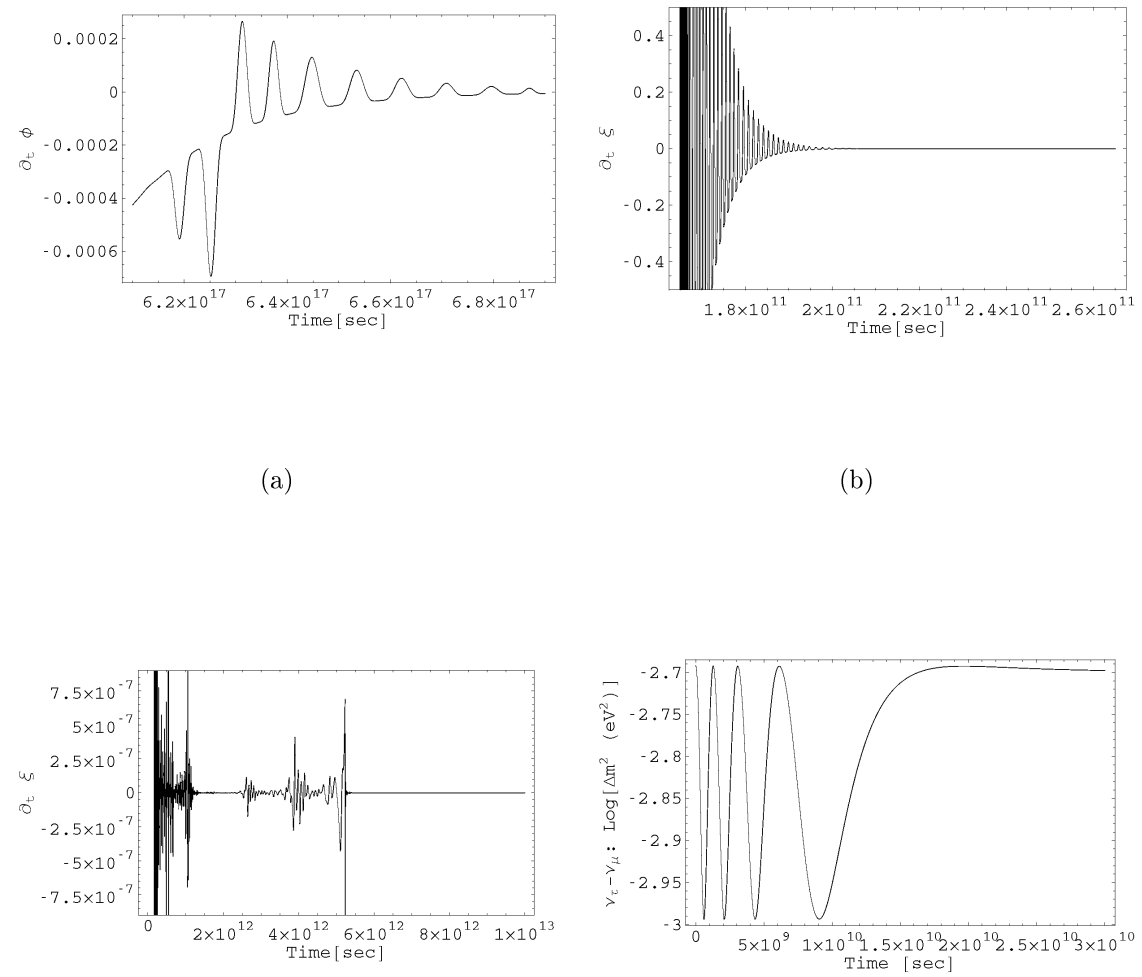

(a) (b)

(c) (d)

Figure 3: Field oscillations and stability of Δm^2 for $(\nu_e - \nu_\mu)$ and $(\nu_\mu - \nu_\tau)$ mixing sectors. Figure (a) exhibits late-time oscillations of the ϕ_i fields about the minima of V_r, which begin at $t \approx 20$ Gyr for physically viable coupling strengths (see discussion below). Figure (b) depicts the rapid oscillation of ξ_i fields in the $(\nu_\mu - \nu_\tau)$ sector. These oscillations decay and become chaotic at late times (c). The oscillation of the mixing mass parameter Δm^2 is shown in Figure (d). These oscillations stabilize at early epochs, and the quantity Δm^2 in this sector never exits the 99% (CL) region reported by the Super Kamiokande experiment [31].

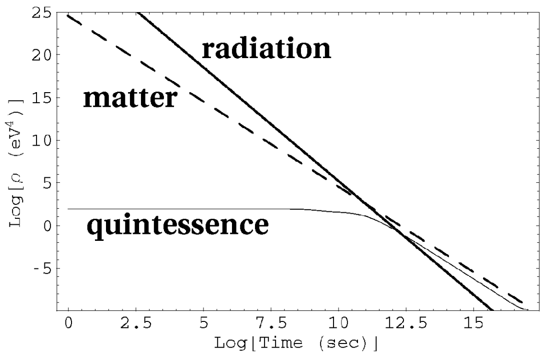

(a)

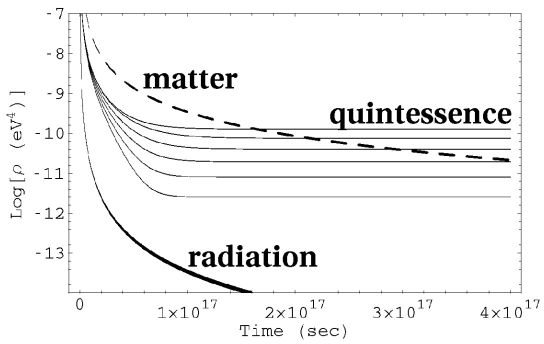

(b)

Figure 4: Energy density evolution for $(\nu_e - \nu_\mu)+(\nu_\mu - \nu_\tau)$ cosmology with background matter and radiation densities of the standard FRW universe. The FRW radiation density is shown as a solid bold line, and the matter density is a dashed bold line. Figure (a) depicts the tracking behavior of ρ_ν (thin solid line) at late times. The contribution ρ_ν is subdominant throughout most of the cosmological history. Figure (b) displays ρ_ν for different m^2 scales against the radiation and matter densities. Starting from the lowest ρ_ν curve (thin solid line), the mass scales are $\Delta m^2 = 2.25 \times 10^{-6},\ 4 \times 10^{-6},\ 6.25 \times 10^{-6},\ 9 \times 10^{-6},\ 1.225 \times 10^{-5}$, and 1.6×10^{-5} eV^2. For this set of coupling strengths, only the three uppermost cases allow ρ_ν to dominate in the present epoch.

4.2 Perturbation spectra

In the standard model of structure formation, small primordial density perturbations in the universe evolved by gravitational instability leading to large-scale structure formation in later epochs. Theoretical spectra can be generated using linear perturbation theory and numerical simulation. Density inhomogeneities in the universe are expressed in terms of the Fourier transform of the spatial matter density fluctuation field [39]:

$$\frac{\delta\rho(\mathbf{x})}{\rho} = \int \frac{d^3k}{(2\pi)^3}\delta(\mathbf{k})\exp(-i\mathbf{k}\cdot\mathbf{x}). \tag{32}$$

The mass power spectrum $P(k)$, which provides an intuitive and comprehensive test of cosmological models, is defined implicitly through its relationship to the *rms* mass fluctuation:

$$\langle\delta(\mathbf{k})\delta^*(\mathbf{k})\rangle = (2\pi)^3 P(k)\delta_{k\bar{k}}(\mathbf{k}-\bar{\mathbf{k}}). \tag{33}$$

In general, cosmological models of primordial scaling fields are viable if early quantum fluctuations in the (non-inflationary) fields do not directly generate density fluctuations for which $\delta\rho/\rho > \mathcal{O}(10^{-4})$. This constraint can either be tested directly, or by indirect comparison with observed power spectra $P(k)$. In Figure 5, I calculate the primordial density fluctuations directly generated by the neutrino fields of the augmented seesaw model. For this model, $|\delta\rho/\rho|$ never exceeds $\mathcal{O}(10^{-45})$. As Δm^2 is increased in the $(\nu_e - \nu_\mu)$ mixing sector, the amplitude of density fluctuations also increases. In Figure 5, Δm^2 is varied from 3.6×10^{-5} eV^2 to 7.225×10^{-5} eV^2.

The power spectrum of primordial mass density perturbations can be discussed for quintessence models in terms of the equation of state w_Q. In Figure 6, power spectra $P(k)$ generated by the augmented Singh model with various w_Q (thin solid curves) are compared with $P(k)$ generated by typical SCDM models (thick solid

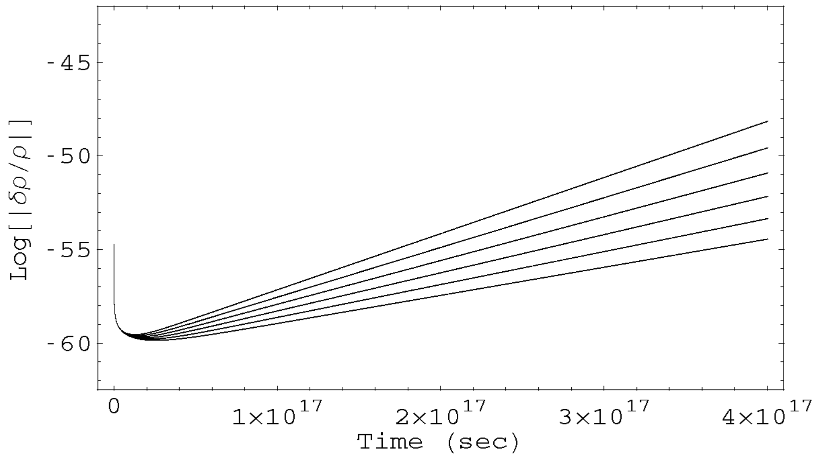

Figure 5: Density fluctuations in the primordial mass field directly generated by neutrino fields in the augmented seesaw model. The mass parameter Δm^2 is varied in the ν_e – ν_μ mixing sector. Beginning at the lower most curve, $\Delta m^2 = 3.6 \times 10^{-5}$ eV^2, 4.225×10^{-5} eV^2, 4.9×10^{-5} eV^2, 5.625×10^{-5} eV^2, 6.4×10^{-5} eV^2, 7.225×10^{-5} eV^2.

curve) and static ΛCDM models (thick dashed curve) subject to conventional COBE normalization. The data points in Figure 6 are based on a large compilation of galaxy clustering surveys by Peacock and Dodds [41]. Starting from the uppermost quintessence spectrum, the neutrino QCDM curves are characterized by $w_Q = -3,\ -2,\ -1.1,\ -0.65,\ -0.3,\ -0.1$. For the upper spectra, w_Q were chosen outside the usual interval $w_Q \in (-1, 0]$ to illustrate the elevation of the overall amplitude beyond $w_Q = -1$. From Figure 6, it is clear that SCDM models generate excess structure on small scales. While the shape of the ΛCDM spectrum is improved relative to SCDM models, the COBE-normalized amplitude generates excess structure on all scales. Since the ability of QCDM models to support long-wavelength fluctuations is controlled by the (constant or effective) equation of state, the overall normalization can be adjusted accordingly. For QCDM models, constraints imposed by the mass power spectrum reduce to constraints on the parameter space that controls the equation of state. In the present study, the spectra in Figure 6 corroborate the parameter constraints quoted in (24 – 27).

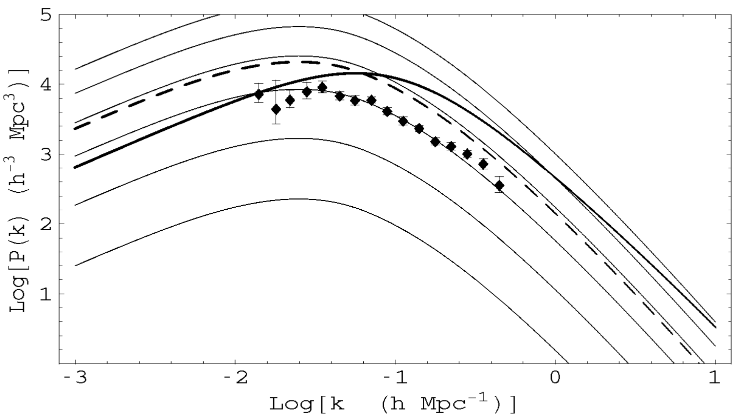

Figure 6: Power spectra for SCDM (thick solid curve), ΛCDM (thick dashed curve), and augmented neutrino QCDM (thin solid curves) models. The data points represent a compilation of galaxy clustering data by Peacock and Dodds [41]. Starting from the uppermost spectrum, the neutrino QCDM curves are characterized by $w_Q = -3,\ -2,\ -1.1,\ -0.65,\ -0.3,\ -0.1$.

4.3 Equation of state

The ability of quintessence models to concur with observation is contained within the equation of state. The instantaneous equation of state, $w_Q(t)$, can be plotted directly. Figure 7 displays the behavior of $w_Q(t)$ for the augmented neutrino QCDM model at late times for varied values of the mass parameter Δm^2. In both plots, the evolution of the neutrino fields in the $(\nu_e - \nu_\mu)$ sector to the minima of V_r appears in the equation of state near $t \approx 10^{16}$ sec, or roughly 300 million years after the Big Bang. At this epoch, $w_Q(t)$ exhibits a rapid shift from $w_Q(t) \simeq 1$ to $w_Q(t) \simeq -1$. The models for which the parameter Δm^2 is smaller undergo this shift at slightly later times. While the shift begins at later times for lighter-mass fields, the overall evolution to $w_Q(t) \simeq -1$ occurs more rapidly for masses up to $\Delta m^2 \approx 1.23 \times 10^{-5}$ eV^2. For mass parameters beyond this threshold, the evolution to $w_Q(t) \simeq -1$ occurs at earlier times and evolves more rapidly.

In Figure 7 (a), the uppermost dotted curve has $\Delta m^2 = 2.25 \times 10^{-6}$ eV^2. The system represented by this curve begins its evolution late, but evolves rapidly to its final value. The lowest dashed-dotted curve represents a system with $\Delta m^2 = 1.6 \times 10^{-5}$ eV^2. This system evolves more rapidly to its VEV than the pattern established by the five lighter systems would indicate. In Figure 7 (b), the uppermost dotted curve was created by setting $\Delta m^2 = 3.6 \times 10^{-5}$ eV^2. Each subsequently lighter system in Figure (b) begins its evolution slightly earlier than the preceding system, evolving more rapidly to its final value. The lowest dashed-dotted curve in Figure (b) is characterized by $\Delta m^2 = 7.225 \times 10^{-5}$ eV^2. For each of the systems depicted in Figure 7, the coupling strengths have been defined to provide an effective equation of state (28) $w_Q \approx -0.65$, as indicated by equation (24).

There are essentially four free parameters in the augmented neutrino QCDM

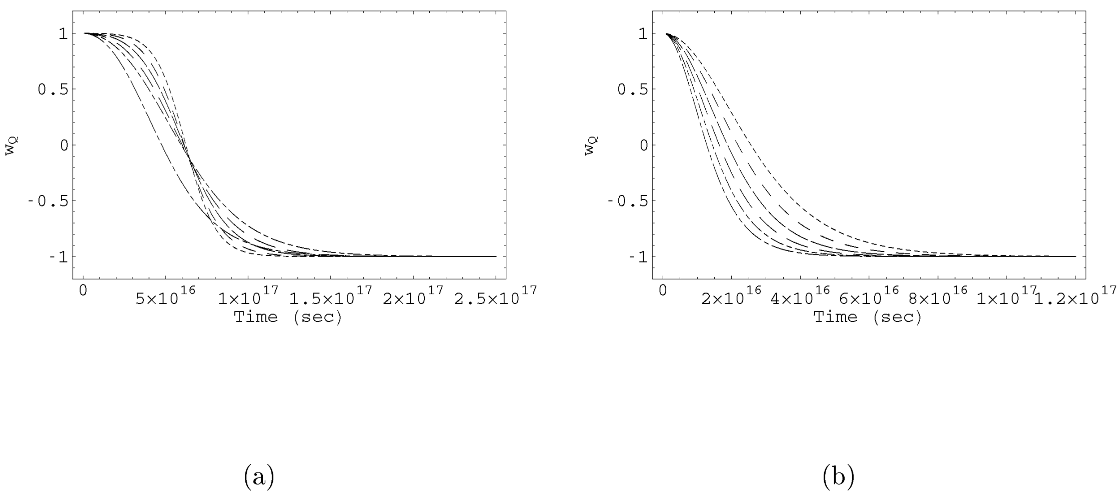

Figure 7: Instantaneous equation of state $w_Q(t)$ for the augmented neutrino QCDM model. Starting from the uppermost dotted curve in Figure (a), the mass mixing parameters are $\Delta m^2 = 2.25 \times 10^{-6}$ eV^2, 4×10^{-6} eV^2, 6.25×10^{-6} eV^2, 9×10^{-6} eV^2, 1.225×10^{-5} eV^2, 1.6×10^{-5} eV^2. Note the change in the established pattern at $\Delta m^2 = 1.225 \times 10^{-5}$ eV^2. Starting from the uppermost dotted curve in Figure (b), the mass parameters are $\Delta m^2 = 3.6 \times 10^{-5}$ eV^2, 4.22×10^{-5} eV^2, 4.9×10^{-5} eV^2, 5.625×10^{-5} eV^2, 6.4×10^{-5} eV^2, 7.225×10^{-5} eV^2. Coupling strengths have been defined to provide an effective equation of state (28) $w_Q \approx -0.65$, as indicated by equation (24).

model: (i) the coupling strength in the $(\nu_e - \nu_\mu)$ mixing sector, (ii) the mass scale Δm^2 in the $(\nu_e - \nu_\mu)$ sector, (iii) the coupling strength in the $(\nu_\mu - \nu_\tau)$ sector, and (iv) the mass scale in the $(\nu_\mu - \nu_\tau)$ sector. As noted in section 4.1, the contribution of the $(\nu_\mu - \nu_\tau)$ sector to the effective equation of state consists of the rapid evolution of the ξ_i fields to their minima and subsequent decay into particles. The portion of this process contributing to the effective equation of state is nearly identical for all physical choices of the mass parameter and coupling strength within the $(\nu_\mu - \nu_\tau)$ sector. Therefore, in terms of the integrated equation of state (28), the model is nearly invariant under physical variations of these parameters.

The contribution of the $(\nu_\mu - \nu_\tau)$ sector to the effective equation of state is plotted directly in Figure 8. The upper solid curve represents the early evolution of the equation of state in the absence of the $(\nu_\mu - \nu_\tau)$ contribution. The lower dashed curve represents the $(\nu_\mu - \nu_\tau)$ contribution at early times. For physical variations in the coupling strength and mass scale in the $(\nu_\mu - \nu_\tau)$ sector, all models converge on the lower curve.

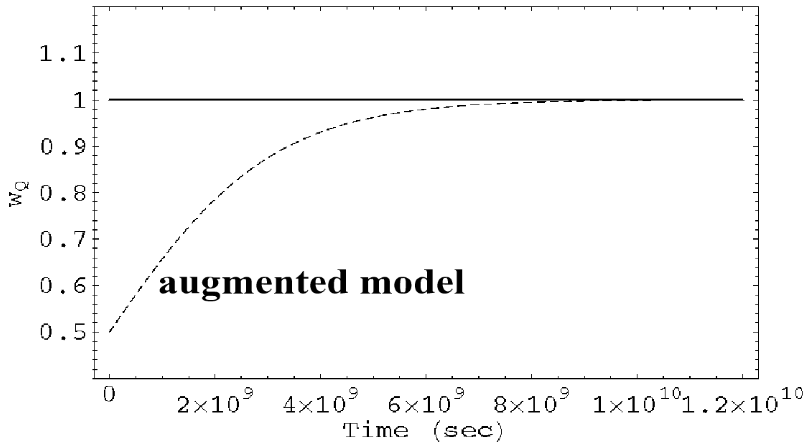

Figure 8: Early evolution of the instantaneous equation of state $w_Q(t)$ for the original Singh model (upper solid curve) and the augmented model (lower dashed curve). For physical variations in the coupling strength and mass scale in the $(\nu_\mu - \nu_\tau)$ sector, all augmented models converge on the lower curve.

Possibly the most important observation of this study is the following: for Δm^2 in the $(\nu_e - \nu_\mu)$ mixing sector chosen within the empirically-allowed regions indicated by neutrino oscillation experiments (see Figure 11 below), the contribution from the $(\nu_\mu - \nu_\tau)$ sector is required if the model is to generate a quintessence scenario for which the effective equation of state lies within $w_Q \approx -0.65 \pm 0.07$ (cf. (24)). The presence of the $(\nu_\mu - \nu_\tau)$ sector lowers the integrated equation of state because of the contribution exhibited in Figure 8. When this contribution is absent, one is forced to raise the coupling strength within the $(\nu_e - \nu_\mu)$ sector exponentially to meet the bounds imposed by equation 24. When the $(\nu_e - \nu_\mu)$ coupling strength is increased, the ϕ_i fields associated with this sector begin to oscillate more rapidly and at earlier epochs, causing the pressure to vanish long before the present time. While the same restrictions apply to the augmented system, the presence of the $(\nu_\mu - \nu_\tau)$ sector extends the allowed region in mass–coupling parameter space to encompass values of Δm^2 allowed by experiment (see Fig. 11) [31].

Figure 9 exhibits restrictions on the parameter space for the augmented neutrino QCDM model. The shaded area below the solid curves are the allowed regions defined by the requirement that the pressure contribution from the $(\nu_e - \nu_\mu)$ sector must be present today. The data points represent iterated values of the mass parameter and coupling strength in the augmented model that generate $w_Q \approx -0.65 \pm 0.07$. In Figure 9 (a), most of these points lie in the excluded region. In Figure 9 (b), the crossover into the allowed region is magnified. The data trend enters the allowed region for $(\Delta m^2)_{\nu_e - \nu_\mu} \approx 1.89 \times 10^{-5}$ eV^2 and $y \approx 0.148$.

The solid constraint curves in Figure 9 define a mass–coupling relationship for the $(\nu_e - \nu_\mu)$ sector that can be extrapolated and plotted against the effective equation of state in w_Q–Δm^2 parameter space. This plot is displayed as the lower solid curve in Figure 10. The allowed region defined in Figure 9 appears as a shaded region below the curve in Figure 10. The allowed region defined by the bit-fit effective equation of state $w_Q \approx -0.65 \pm 0.07$ appears in Figure 10 as a horizontal green bar between the values $w_Q = -0.72$ and $w_Q = -0.58$. The central best-fit equation of

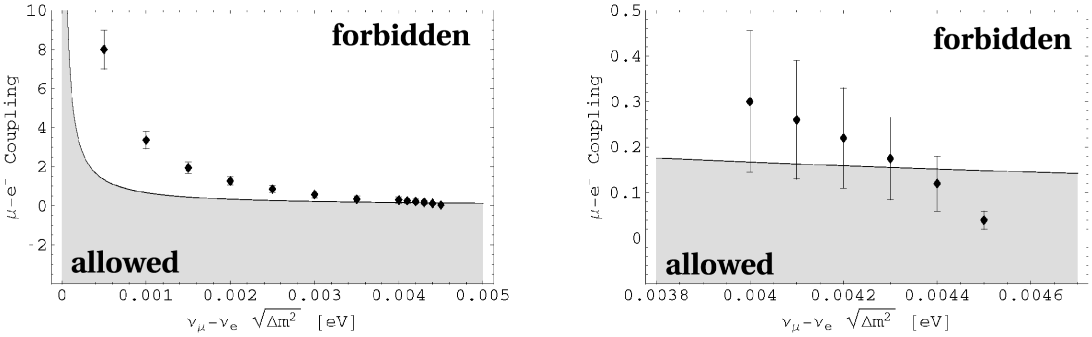

(a) (b)

Figure 9: Constraints on parameter space for the augmented neutrino QCDM model. The shaded regions below the solid curves represent the allowed region defined the requirement that the acceleration driven by the $(\nu_e - \nu_\mu)$ sector must be present today. The data points represent iterated values of the mass parameter and coupling strength that generate $w_Q \approx -0.65 \pm 0.07$. In Figure (a), most of these points lie in the excluded region. Figure (b) displays the crossover into the allowed region by the mass–coupling strength relationship.

state $w_Q = -0.65$ is marked by a thick dotted line. The shaded region between $w_Q = -1$ and $w_Q = -0.2$ represents the total allowed range of the effective equation of state defined by the 2σ confidence region that combines low redshift surveys, CMB anisotropy data, and spectral and photometric measurements of type Ia supernovae [7]. The small mixing angle (SMA) and large mixing angle (LMA) regions (in blue) between the mass scales 3×10^{-6} eV$^2 \lesssim \Delta m^2 \lesssim 9 \times 10^{-6}$ eV^2 and 2.6×10^{-5} eV$^2 \lesssim \Delta m^2 \lesssim 2.8 \times 10^{-5}$ eV^2 represent combined neutrino oscillation data from Homestake, SAGE, GALLEX, Kamiokande, and Super Kamiokande, plus electron recoil energy spectra and the day – night effect observed over 825 days at Super Kamiokande [32]. The SMA region encompases the 90% CL sector of the MSW plane, while the LMA region shows the centroid value of the 99% CL sector. The best-fit solution for the augmented neutrino QCDM model appears as a dark blue overlap area marked as the auper-allowed region (SAR). Although neutrino oscillation data does not warrant a best-fit equation of state ($-0.72 \leq w_Q \leq -0.58$) for centroid LMA masses, allowed LMA values of Δm^2 fall within the 2σ region $-1 \leq w_Q \lesssim -0.2$. The constraints deppicted in Figure 10 favor SMA neutrino mass eigenstates.

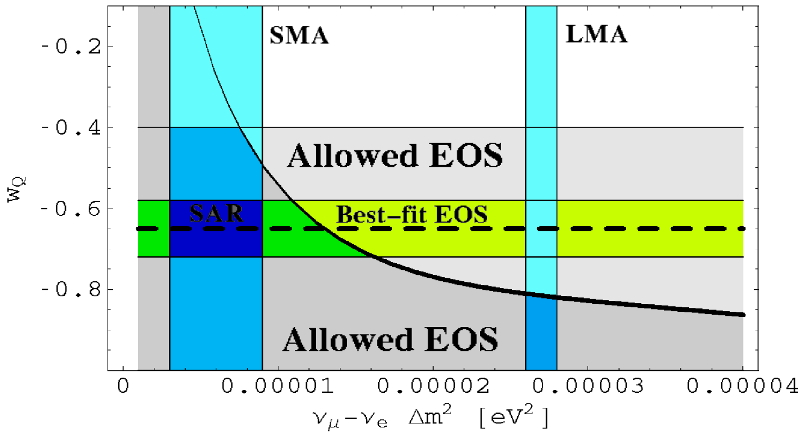

Figure 10: Crossover of allowed regions in (w_Q – Δm^2) parameter space. Allowed regions are defined by small mixing angle (SMA) and large mixing angle (LMA) neutrino oscillation measurements, low redshift surveys, CMB anisotropy observations, type Ia supernovae surveys, and requirements on the presence of a pressure contribution from the (ν_e – ν_μ) mixing sector. The super-allowed region (SAR) favors SMA neutrino mass eigenstates. The 2σ allowable region (Allowed EOS) appears in grey in the interval $-1 \leq w_Q \leq -0.4$. LMA centroid values meet observational constraints at the 2σ level.

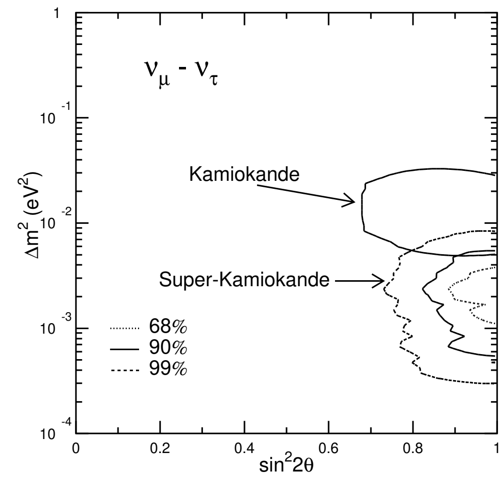

(a)

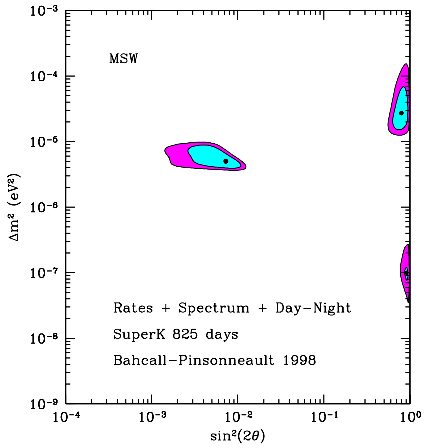

(b)

Figure 11: Results from neutrino oscillation experiments [31]. Figure (a) represents $(\nu_\mu - \nu_\tau)$ mixing data collected from the Kamiokande and Super Kamiokande experiments. The 99% (CL) region corresponds roughly to the mass range 9×10^{-3} eV$^2 \lesssim \Delta m^2 \lesssim 3 \times 10^{-2}$ eV^2. Figure (b) [32] represents combined $(\nu_e - \nu_\mu)$ mixing data from GALLEX, SAGE, Homestake, and Super Kamiokande, plus electron recoil energy spectra and the day – night effect observed over 825 days at Super Kamiokande. The shaded regions represent global solutions for the allowed oscillation regions in the MSW solution. The small mixing angle (SMA) region corresponds to the mass range 3×10^{-6} eV$^2 \lesssim \Delta m^2 \lesssim 9 \times 10^{-6}$ eV^2. The large mixing angle (LMA) centroid value is $\Delta m^2 = 2.7 \times 10^{-5}$ eV^2. The other solution is known as LOW. The CL contours correspond to $\chi^2 = \chi^2_{min} + 1.61(9.21)$. The outer solid contours represent 90% CL regions, while the inner contours mark 99% CL regions.

4.4 Tracking behavior

The renormalized effective potential for the neutrino QCDM model (eqn. 10) does not meet the conditions for tracking solutions outlined in Section 3. In general, potentials that support field oscillations do not admit tracking behavior [42]. The evolution of fields in the potential V_r and the behavior of the vacuum energy density contribution (18), however, can be searched directly for *pseudo*-tracking solutions.

Figure 12 displays field evolution and vacuum energy density behavior for a set of equal-mass, equal-coupling quintessence fields with widely varied initial conditions. Figure 12 (a) shows the convergence of three such quintessence fields over a time scale of $0 \leq t \lesssim 7 \times 10^4$ sec. The initial field values in Figure (a) span 50 orders of magnitude. While pure tracking solutions admit convergence for initial conditions that span more than 100 orders of magnitude, the fields in the present model become sensitive to initial choices of $\dot{\phi}_i(0)$ and $\dot{\xi}_i(0)$ when $\phi_i(0)$ and $\xi_i(0)$ span more than ≈ 50 orders of magnitude.

Figures 12 (b) – (d) depict converging energy density contributions from six quintessence fields with widely varied initial conditions. Initial field values span roughly 50 orders of magnitude. Within this range, $\dot{\phi}_i(0)$ and $\dot{\xi}_i(0)$ were chosen to span more than 200 orders of magnitude. Figure 12 (b) shows five of the six quintessence fields converging to a common track by $t \approx 10^9$ sec. The last field oscillates about its attractor. These oscillations (Fig. 12 (c) – (d)) stabilize near $t \approx 10^{13}$ sec.

For initial field values chosen within a range of roughly 28 orders of magnitude, convergence is more certain, and takes place at very early times. Figure 13 displays this convergence of energy density contributions from four quintessence fields whose initial values span 25 orders of magnitude. Tracking behavior is clear in these fields as early as $t \approx 0.5$ seconds after symmetry breaking.

The region of initial field values within which pseudo-tracking solutions are exhibited can be mapped by observing a large range of energy density contributions from equal-mass, equal-coupling quintessence fields. Figure 14 depicts the behavior of various energy density contributions from the present model (thin solid lines) chosen to span roughly 27 orders of magnitude at early times. The FRW matter and radiation densities appear as thick dashed and solid lines, respectively. For initial contributions in the interval $\mathcal{O}(10^1\ \mathrm{eV}^4) \lesssim \rho_{\mathrm{vac}} \lesssim \mathcal{O}(10^{20}\ \mathrm{eV}^4)$, energy densities generated by the augmented neutrino QCDM model converge to a common track just after the equivalence epoch. For energy density contributions with initial values below $\rho_{\mathrm{vac}} \approx \mathcal{O}(10^{-1}\ \mathrm{eV}^4)$, the solution diverges and the resulting cosmology is not viable.

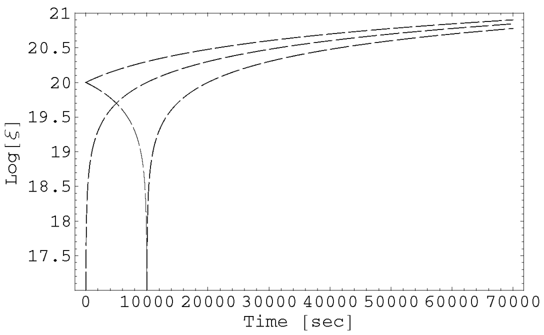

(a)

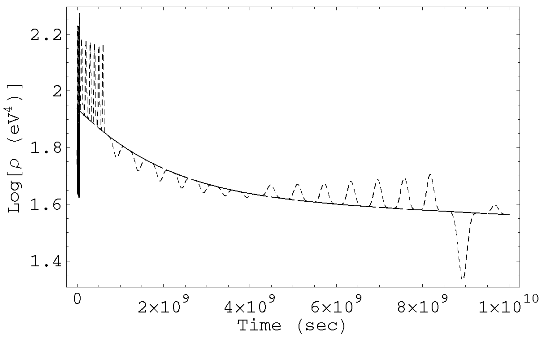

(b)

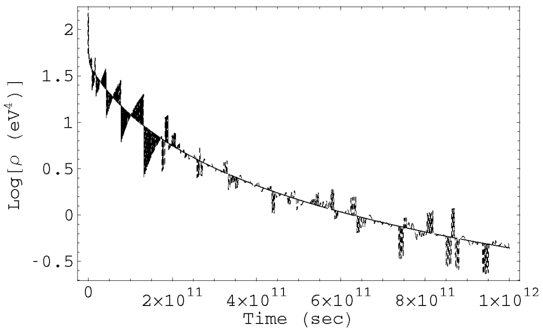

(c)

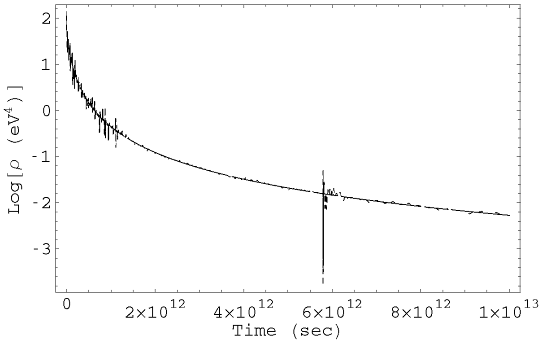

(d)

Figure 12: Pseudo-tracking behavior in equal-mass, equal-coupling quintessence fields in the present model. Figure (a) depicts dynamical convergence of the fields themselves out to $t \approx 10^5$ sec. Figures (b) – (d) depict convergence of energy density contributions from six fields with initial field values chosen to span roughly 50 orders of magnitude. Five of the six fields converge to a common track at early times. One field oscillates about its attractor and converges near $t \approx 10^{13}$ sec.

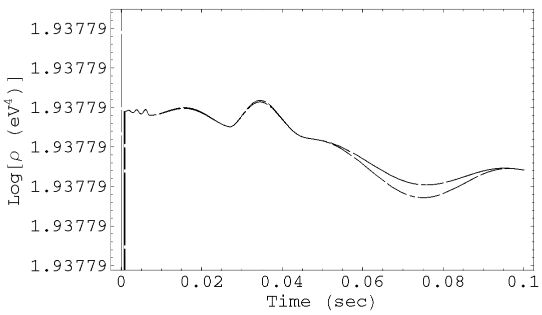

(a)

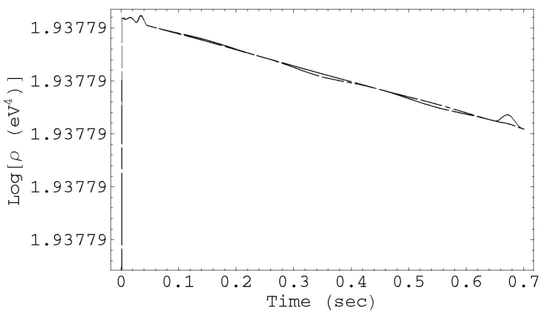

(b)

Figure 13: Converging energy density contributions from four equal-mass, equal-coupling quintessence fields in the present model. Convergence occurs as early as $t \approx 0.5$ seconds after symmetry breaking.

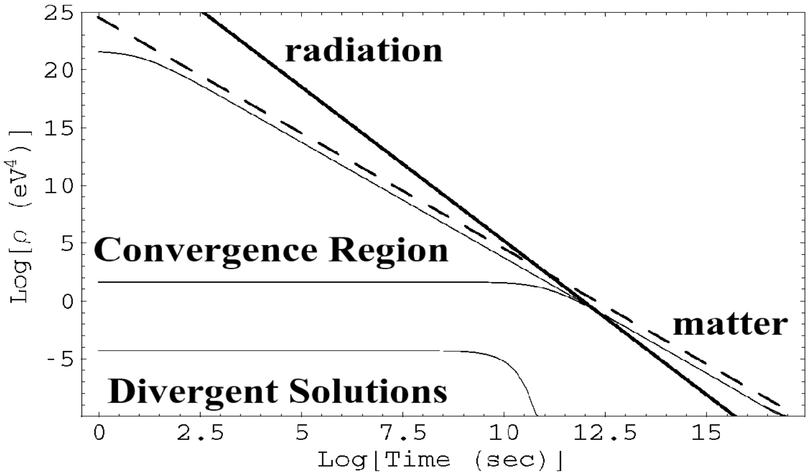

Figure 14: Energy density contributions from equal-mass, equal-coupling quintessence fields in the present model. For initial contributions in the interval $\mathcal{O}(10^1\ \mathrm{eV}^4) \lesssim \rho_{\rm vac} \lesssim \mathcal{O}(10^{20}\ \mathrm{eV}^4)$, energy densities generated by the augmented neutrino QCDM model converge to a common track just after the equivalence epoch. For energy density contributions with initial values below $\rho_{\rm vac} \approx \mathcal{O}(10^{-1}\ \mathrm{eV}^4)$, the solution diverges and the resulting cosmology is not viable. The FRW matter and radiation densities appear as thick dashed and solid lines, respectively.

5 Discussion

The physical and observational constraints on the augmented seesaw QCDM model can be summarized as: (i) the pressure contribution from the $(\nu_e - \nu_\mu)$ mixing sector must be present today, (ii) the mixing parameter Δm^2 is, for small-angle mixing, restricted to the interval 3×10^{-6} eV$^2 \lesssim \Delta m^2 \lesssim 9 \times 10^{-6}$ eV^2 (see Fig. 11) [31], (iii) the effective equation of state must lie in the 2σ region $-1 \leq w_Q \lesssim -0.2$, acquired from low redshift surveys, CMB anisotropy measurements, and type Ia supernovae observations [7], and (iv) solutions should address the problems of cosmological coincidence and fine-tuning. The original SU(2) seesaw model proposed by Singh to generate acceleration in the present epoch is excluded under these constraints. The model requires the presence of a similar but independent SU(2) seesaw mechanism in the $(\nu_\mu - \nu_\tau)$ mixing sector to lower the effective equation of state without requiring exponentially large couplings in the $(\nu_e - \nu_\mu)$ sector (see Fig. 9). With this additional system present, the resulting QCDM model favors SMA neutrino mass eigenvalues (see Fig. 10). Although the LMA centroid value does not admit best-fit solutions, $(-0.72 \leq w_Q \leq -0.58)$ [7], it is still an allowable solution in terms of constraint (iii).

The augmented seesaw model presents a natural approach to the problem of fine-tuning, generating energy densities in the present epoch proportional to the fourth power of the fundamental mass scale of the system. The model also addresses the problem of cosmic coincidence by exhibiting pseudo-tracking behavior. The quintessence fields generated in the augmented neutrino QCDM model exhibit convergence for initial vacuum energy density contributions in the range $\mathcal{O}(10^1 \text{ eV}^4) \lesssim \rho_{\text{vac}} \lesssim \mathcal{O}(10^{20} \text{ eV}^4)$. While these quintessence fields do not generate pure tracking solutions, the tracking behavior observed (Fig. 12 – 14) is highly insensitive to initial conditions over roughly 28 orders of magnitude. This represents a significant improvement over non-tracking models that often require fine tuning to nearly 1 part in 10^{120} [12]. Furthermore, the augmented seesaw model is highly insensitive to physical changes in the mass parameter and coupling strength associated with the $(\nu_\mu - \nu_\tau)$ mixing sector, reducing the free parameters in the problem from four to two.

The present study has shown that the augmented neutrino model of QCDM cosmology is a physically motivated and cosmologically viable solution to the missing-energy problem. In light of recent advancements in the parameterization of quintessence and tracking models, theoretical cosmology may expect significant developments in the search for a well motivated particle physics model of tracking QCDM. New experiments, including those designed to generate precision measurements of CMB anisotropies, will significantly improve constraints on the parameter space of such models, and future theories should attempt to meet current and future best-fit scenarios. Perhaps the neutrino mass hierarchy will again be exploited in the selatearch for a physical model of tracking QCDM.

Acknowledgements: The author wishes to thank Prof. Marc Sher for his warm mentorship and guidance, and Prof. Paul Steinhardt for his helpful conversation, correspondence, and hospitality.

A Casimir Energy in Astrophysics: Gamma-Ray Bursts from QED Vacuum Transitions

Abstract

Motivated by analogous applications to sonoluminescence, neutron star mergers are examined in the context of Schwinger's dynamical Casimir effect. When the dielectric properties of the QED vacuum are altered through the introduction of dense matter, energy shifts in the zero-point fluctuations can appear as photon bursts at gamma-ray frequencies. While many gamma-ray burst models face significant problems associated with baryon-rich radiation environments, a theory dependent upon extreme baryon loading at the emission site arises naturally from the application of Casimir dynamics to sudden dielectric transitions on astrophysical scales. The amount of radiation depends upon the properties and amount of matter in motion and the suddenness of the transition. It is shown that the dynamical Casimir effect can convert sufficient energy of neutron star mergers into gamma rays. Using information extracted from simulations of matter flow in neutron star mergers by Ruffert and Janka, we estimate that the total Casimir energy released can exceed 10^{53} ergs in gamma-ray frequencies. The Casimir energy approach is capable of explaining the most energetic gamma-ray bursts.

A.1 Introduction

In a recent series of calculations involving the dynamical Casimir effect, Schwinger and others have shown that a rapid shift in the zero-point energy of the QED vacuum generates electromagnetic radiation [43, 44, 45]. This effect may be observed on a terrestrial scale in the form of sonoluminescence, wherein acoustic vibration of water bubbles produces flashes of visible light. Renewed interest in Schwinger's dynamical Casimir effect has revealed that electromagnetic energy promoted from QED vacuum fluctuations is dependent upon a volume term at first order. The implications of this result are momentous in the context of astrophysical phenomena.

The dynamical Casimir mechanism is straightforward. The zero-point modes of the QED vacuum are characterized by a minimum energy per wavenumber of $(1/2)\hbar\omega$. When a vacuum field configuration is altered through the introduction of a dielectric, the zero-point energy of the system is reduced by a factor of $(1/\sqrt{\epsilon})$ per mode. The dielectric constant ϵ is normally frequency dependent, and characterizes the energy contribution from each wavenumber. For sudden transitions, the difference in zero-point energies invoked by dielectric damping is radiated away as photons. The Casimir energy of a dynamic system is thus defined as the change in zero-point energy due to a change in the environment. This energy is dependent upon volume and, at least in simple models for the frequency dependence of ϵ, upon the fourth power of a high-frequency cutoff. Attempts have been made to show that the bulk energy contribution is several orders of magnitude smaller than that conveyed by volume dependence, e.g. [46]. These attempts have been successfully countered in several papers, including those by Liberati *et al.* [44, 45] and Carlson *et al.* [47].

In the realm of astrophysics, the dynamical Casimir effect is important whenever vacuum is replaced with extremely dense material over short time scales. Supernovae, binary mergers, neutron star-quakes, and other events are capable of producing Casimir radiation. The volume and high-frequency dependence of the Casimir mechanism implies immense energy production in the form of photons, making it a useful hypothesis in the study of unexplained energy bursts. The suggestion to employ Casimir physics in a theory of gamma-ray bursts (GRBs) was first made by Carlson *et al.* [48], where it was shown that the dynamical Casimir effect can convert the energy of neutron star-quakes into gamma rays. Such events would require approximately 10^{40} ergs of source energy in the form of Casimir radiation to produce the fluences seen on earth. The star-quake solution to GRBs was suggested before several red shifts of optical transients associated with GRB's were measured, and assumes a distance scale on the order of 10^5 pc. It is currently believed, however, that GRBs originate at cosmological distances [49].

To formulate a theory of cosmological GRBs, it is sensible to consider the Casimir mechanism in a broader array of astrophysical phenomena. It is widely postulated that binary neutron star mergers provide the energy source for GRBs. Time scales and structures of burst spectra indicate sources no larger than a few tens of kilometers in diameter [50]. Calculations have also shown that the predicted rate of neutron star mergers in our Hubble volume is comparable to the detection rate of GRBs [51]. The mechanism by which the gravitational energy of a binary neutron star system is converted to electromagnetic radiation during the collapse of the system remains an open question. In addition, conversion mechanisms must efficiently generate photons in the gamma-ray energy range. The dynamical Casimir effect may provide such a mechanism.

When binary neutron star systems decay and two neutron stars merge, tremendous volumes of dense material are ejected at relativistic speeds into the vacuum surrounding the collision site. As vacuum is rapidly replaced with dielectric, the Casimir mechanism converts the energy of the binary merger into photons. The frequency of Casimir-induced radiation is determined by the statistical properties of the media involved. For neutron-star matter, gamma-rays arise naturally from simple representations of the plasma frequency ω_p. Stated simply, current understanding of the Casimir mechanism implies electromagnetic radiation bursts from neutron star mergers. The theoretical properties of these bursts must be compared with the observed characteristics of GRBs.

GRBs are detected [50] as brief energy fluxes on the order of 10^{-4} to 10^{-8} erg cm^{-2} s^{-1} in the $50 - 300$ keV energy range. Flux durations are distributed bimodally, peaking at ≈ 0.3 sec. and ≈ 25 sec. Photons are detected at energies from several keV to tens of MeV. Occasionally, photon energies reach hundreds of MeV [52]. Assuming standard cosmologies in conjunction with observed red shifts of GRB optical transients ($z \approx 1$ up to ≈ 3.4, $H_0 = 65$ km s^{-1} Mpc^{-1}), the total energy released at the source of a GRB must range from $E_{source} \approx 10^{49}$ ergs up to $\approx 10^{54}$ ergs. Unless there are two separate energy classifications of GRBs, any model attempting to explain this phenomenon must accommodate these luminosities.

The essential goal of this paper is to suggest a consistent theory of GRBs in which the bulk energy contribution is provided by the Casimir mechanism. Binary neutron star mergers are the focus of this study, though smaller *Casimir bursts* generated by other astrophysical events are also possible. In section 1.2, a brief review of the dynamical Casimir effect is presented. The properties of Casimir-induced GRBs are discussed in section 1.3.

A.2 Dielectric Transitions in the QED Vacuum

The Casimir approach to sonoluminescence originated in a series of papers by Schwinger [43]. Although he classified his approach as *dynamical*, Schwinger's essential argument was a comparison of two steady state field configurations. Subsequent studies have confirmed Schwinger's result in the sudden transition approximation [44]. These treatments, partly inspired by an ongoing controversy regarding sonoluminescence, have brought a more detailed understanding of efficiency and time-dependent transition dynamics to Schwinger's original strategy.

Schwinger derived a concise expression for the energy (per polarization state) associated with a collapsing vacuum cavity embedded in a uniform dielectric slab. The dominant energy contribution is given by the first order term, dependent upon a quantization volume V:

$$E_{Casimir} = V \int \frac{d^3\mathbf{k}}{(2\pi)^3} \frac{1}{2} \hbar ck \Big(1 - \frac{1}{\sqrt{\epsilon(k)}}\Big). \tag{34}$$

Additional terms appear as finite volume corrections proportional to the surface area of the dielectric [53]. When the dielectric is large relative to wavelengths of emitted Casimir photons, these finite volume contributions are insignificant.

The integral in (34) can be understood through the introduction of a high-frequency momentum cutoff K. Physically, this cutoff describes the asymptotic behavior of the dielectric parameter $\epsilon(k)$ at high wavenumbers. At high frequencies, $\epsilon(k)$ drops to unity and the dielectric dispersion relation becomes that of the vacuum. In the case of neutron star matter, this high-frequency cutoff is closely related to the plasma frequency ω_p; K determines the scale at which electrons in plasma no longer react to oscillating electromagnetic fields. Since a neutron star is essentially a metal in terms of dielectric properties, it is sensible to set $\epsilon(k) \to \infty$ for all k corresponding to frequencies below the cutoff parameter K. Summing over polarization states, equation (34) becomes

$$\begin{aligned} E_{Casimir} &= V \int_0^K \frac{d^3\mathbf{k}}{(2\pi)^3} \hbar ck \Big(1 - \frac{1}{\sqrt{\epsilon}}\Big) && (35) \\ &= V \int_0^K dk \frac{1}{2} \frac{4\pi k^3}{(2\pi)^3} \hbar c \Big(1 - \frac{1}{\sqrt{\epsilon}}\Big) && (36) \\ &= \frac{V}{8\pi^2} \hbar c K^4 \Big(1 - \frac{1}{\sqrt{\epsilon}}\Big). && (37) \end{aligned}$$

Equation (35 – 37) expresses, in the sudden-transition limit, the energy available for radiation after a volume of vacuum experiences a dielectric transition. The simplest interpretation of (37) is that the Casimir energy is obtained by summing the difference in dispersion relations of the 'in' and 'out' field configurations over the density of states. This view is corroborated in ref. [47], where Carlson *et al.* used an elementary application of quantum field theory. In their approach, homogeneous dielectrics were treated as distortions in Minkowski space with a flat-space background. In place of a fixed three-momentum cutoff, time splitting was used to approximate a sharp change in dielectric behavior. A more extensive calculation from first principles is also possible [47].

It is also easy to verify that the Casimir energy expressed in (37) appears in physical systems as electromagnetic radiation. The original field configuration may be expressed in terms of the final configuration plus excitations representing pairs of photons propagating with equal momenta in opposite directions. This is the approach presented in [44, 45], wherein Maxwell's equations provide a simple equation of motion for the photon gauge field. Under this formalism, separate field configurations of in and out states correspond to different quantization bases. Through an explicit calculation of the Bogoliubov coefficients that relate separate field configurations, it is possible to compute the number and energy spectrum of a generic system. By introducing a time-dependent transition profile, energy production efficiency may be correlated with various time-dependent parameters of the system. Using this technique, Liberati *et al.* were able to show that Casimir-induced radiation at a given frequency ω is suppressed by a factor $\exp(-\omega t_0)$, where t_0 is the time scale of the transition. Thus, dielectric transitions must be relativistic for the Casimir mechanism to be a significant energy source. This property of the dynamical Casimir effect is independent of the time-dependent transition profile chosen for ϵ.

A.3 Burst Mechanism

Due to growing interest in neutron star mergers as possible sources of GRBs, efforts to analyze merger dynamics computationally have given rise to several detailed simulations. In a sequence of papers by Ruffert *et al.*, binary mergers were simulated with an Eulerian PPM (piecewise-parabolic method) code using both off-center and head-on collision scenarios [54]. These three-dimensional simulations will provide the basis for many of the parameter values chosen in the present calculation. In [54], Ruffert *et al.* studied the merger properties of a collapsing binary system composed of two $1.6M_{\odot}$ neutron stars with radii $R = 15$ km. Although several different models were used to simulate neutron star mergers, many generic parameters emerged from these studies. What follows is a brief summary of a typical merger scenario based on the work of Ruffert *et al.*.

During a neutron star merger, large volumes of matter escape each neutron star and fill the surrounding vacuum. Matter is ejected into a toroidal accretion disk with an outside radius of approximately 150 km. The merger remnant, which collapses to a black hole on a time scale of a few milliseconds, is approximately 40 km in diameter. The system reaches a quasi-static state after several ms, at which time the accretion torus maintains a relatively stable mass that ranges from several 10^{-2} $M_{\odot}$ to a few 10^{-1} $M_{\odot}$. The angular momentum of the accretion torus prevents its collapse into the merger remnant. The total volume of the torus reaches several 10^{21} cm^3, with maximum densities of $\approx 10^{14}$ g cm^{-3}. The innermost region of the torus is roughly 45 km thick, extends approximately 70 km from the center of the merger site, and is characterized by an average mass density of $\rho \approx 10^{11.8}$ g cm^{-3}. Beyond this region, the density decreases steadily, dropping to $\rho \approx 10^{9.5}$ g cm^{-3} at a radial distance of 150 km from the center of the merger remnant. The mass accretion rate of the black hole remnant peaks at several solar masses per ms, but is generally characterized by several 10^{-2} $M_\odot$ s^{-1} after a quasi-static state is reached. Radial velocities of matter on the equatorial plane (relative to the speed of light) reach 10^{-1} c at a radial distance of 80 km and t $\approx$ 15 ms after the beginning of the merger. Just after the collapse of the system, however, matter is ejected outward at speeds approaching several 10^{-1} c. The ratio of electrons to baryons in the accretion torus ranges from an electron fraction of roughly $Y_e \approx 0.02$ at the outermost edges, to $Y_e \approx 0.30$ just inside the outer shell. After the first few ms of the merger, most of the material within the outer shell of the accretion torus has an electron fraction ranging from $Y_e \approx 0.06$ to $Y_e \approx 0.10$. At early times in the merger, material ejected into vacuum is composed mainly of large volumes encapsulated in shells of higher electron fraction and higher mass density (relative to material within the volumes). For head-on collisions, these shells reach densities of $\rho \approx 10^{14}$ g cm^{-3} with electron fraction $Y_e \approx 0.40$. For off-center collisions, these shells are characterized by $\rho \approx 10^{12}$ g cm^{-3} and $Y_e \approx 0.10$.

What is relevant to the Casimir mechanism is the replacement of vacuum with dielectric at relativistic transition rates. This situation is most apparent in the creation of the accretion torus during a neutron star merger. It is helpful to simplify the merger scenario in terms of events that contribute to Casimir-induced radiation. For the present calculation, I will consider the first few ms of a neutron star merger to be composed of two steps: (i) encapsulated matter with outer-shell densities of $\rho \approx 10^{11.8}$ – 10^{14} g cm^{-3} and electron fraction $Y_e \approx 0.02$ – 0.40 is ejected at radial speeds approaching $0.85c$ from the merger site, and (ii) this matter soon occupies an accretion volume roughly equal to 10^{21} cm^3.

As mentioned above, the suppression factor $\exp(-\omega t_0)$ implies a need for sudden transitions. Supposing that (up to the cutoff frequencies) the transition is sufficiently rapid, this factor does not play a significant role. Such an assumption is indeed a valid approximation in the merger scenarios presently considered.

As neutron star matter moves into vacuum regions at relativistic speeds during a merger, Casimir energy is released from the interaction region of matter and vacuum. Since Casimir-induced radiation appears as photons propagating in opposite directions, half of the photons released from the merger are directed inward toward the merger remnant. Thus, the Casimir energy released from a merger is suppressed by another factor of 1/2 (or a bit more, as the out-flowing matter can catch photons that emerge outward at oblique angles). Otherwise, photons are directed outward into vacuum, and baryon loading at the emission site is not a serious concern. In fact, the high mass densities associated with neutron star mergers imply an extremely high frequency cutoff K. Including the factor 1/2 and taking $\epsilon_{neutronstar} \rightarrow \infty$ up to K, the Casimir energy radiated outward from a typical neutron star merger is:

$$E_{Casimir} = \frac{1}{2}\frac{V\hbar c K^4}{8\pi^2} \tag{38}$$

$$\approx 1.3 \times \left[\frac{K(\mathrm{MeV}/c)}{100(\mathrm{MeV}/c)}\right]^4 \times \left[\frac{V}{10^{21}\mathrm{cm}^3}\right] \times 10^{53}\mathrm{ergs}. \tag{39}$$

Various methods for estimating the cutoff parameter K are available. With photon spectra from some GRBs reaching few $\times$ 10 MeV [50, 52], it is reasonable to assume $\hbar c K$ is slightly larger. Physically, the cutoff parameter is closely related to the plasma frequency:

$$\omega_p = \sqrt{\frac{4\pi n_B Y_e e^2}{m_e}}. \tag{40}$$

The plasma frequency determines the energy scale at which a dielectric plasma no longer responds to external electromagnetic fluctuations, and is dependent upon the electron fraction Y_e, the baryon number density n_B, and the electron mass m_e. The simulation parameters provided by Ruffert *et al.* indicate that the matter ejected into vacuum at early times in a merger can be characterized by $Y_e \approx 0.40,\ n_B \approx \mathrm{few} \times 10^{37}$.

These parameters yield a cutoff of $\hbar c K \approx \hbar \omega_p$ close to 100 MeV. These independent estimates of the cutoff wavenumber are consonant with observed properties of GRBs. From equation (39), it is clear that the Casimir energy is sensitive to the cutoff parameter, and most of the energy emitted from a merger event lies in the frequency region just below K.

A more accurate calculation for the number spectrum can be done using the formalism employed by Liberati *et al.* [44, 45]. The number spectrum is obtainable through an explicit calculation of Bogoliubov coefficients relating separate vacuum states of a dynamic system. A simple equation of motion may be derived from Maxwell's equations. By introducing a convenient time-dependent profile for the refractive index, the problem is tractable. These spectra reveal the sensitivity of the Casimir mechanism to the time scale of the dielectric transition. Calculation of Bogoliubov coefficients can be used to test the validity of the Casimir approach when detailed underlying spectral curves of GRBs become available. Using equation (39) in conjunction with the simulation-based NS merger parameters suggested by [54], it is clear that the Casimir mechanism can produce energy bursts approaching 10^{53} ergs. Since Casimir photons are emitted from the interaction region of matter and vacuum, most of the calculated energy in this scenario escapes the merger site.

A.4 Discussion

The central result of this paper is that the Casimir mechanism is a candidate explanation of cosmological GRBs. Even when time-dependent transition scenarios are encountered, Schwinger's dynamical Casimir effect accounts for GRBs releasing a few $\times 10^{53}$ ergs at the source. This energy is sensitive to estimates of a cutoff parameter K and the volume of matter involved in a typical merger. Various beaming effects may improve the Casimir mechanism even further. Even if the estimates in this paper are grossly incorrect, however, the Casimir mechanism should not be abandoned. Using the most conservative (but still rational) parameters, a quasi-static comparison of the 'in' and 'out' states of a NS merger at $t < 0$ and $t \approx 15$ ms (with appropriate suppression factors) gives $E_{Casimir} \approx 10^{51}$ ergs. This energy scale accounts for many of the smaller observed GRBs.

While it is possible to generate large GRBs by the Casimir mechanism, many aspects of this theory must be addressed. We employed a model where $\epsilon(k)$ was significantly larger than unity and essentially constant even at frequencies approaching $k = K$. Further efforts are underway to conduct a calculation of $\epsilon(k)$ for neutron star matter based on first principles. The basic approach is to begin with a simple equation of motion, introduce specific waveforms at the matter-vacuum interaction region, and allow these waves to propagate. While similar calculations exist for terrestrial applications, the dielectric properties of an extremely dense plasma are not well understood.

The current calculation relies on generalized conditions derived from the computer simulations of Ruffert *et al.* [54]. Many of the crucial diagrams in these papers represent times in the merger of $t \approx 1.4$ ms and $t \approx 15$ ms. For more accurate estimates of the Casimir energy involved in a neutron star merger, detailed information is required from very early times in the merger ($0 \leq t \leq 1$ ms). The estimates made in the present calculation were based on reasonable extrapolations. The fine structure properties and durations of GRBs depend upon the detailed dynamics of neutron star mergers. Again, appropriate information from simulations may corroborate the candidacy of the Casimir mechanism as a source of GRBs. GRBs generated by the Casimir mechanism also rule out the possibility of repeating burst scenarios. There is little evidence for repeating GRBs, though efforts continue to discover 'repeaters' in GRB sky maps [55].

Acknowledgments: IJS thanks S. Liberati for conversations and hospitality on a visit to SISSA (Trieste, Italy), the Charles Center of the College of William and Mary for a Monroe grant, the Barry M. Goldwater Foundation for support.

References

[1] J. P. Ostriker and P. J. Steinhardt, Nature **377**, 600 (1995).

[2] D. O. Caldwell, hep-ph/9910349.

[3] J. R. Primack, J. Holtzman, A. Klypin and D. O. Caldwell, Nucl. Phys. Proc. Suppl. **43**, 133 (1995).

[4] A. Guth, Phys. Rev. **D23**, 347 (1981).

[5] A. Linde Phys. Rev. Lett. **108B**, 389 (1982).

[6] A. Albrecht, P. Steinhardt Phys. Rev. Lett. **48**, 1220 (1982).

[7] L. Wang, R. R. Caldwell, J. P. Ostriker and P. J. Steinhardt, Astrophys. J. **530**, 17 (2000) [astro-ph/9901388].

[8] A. D. Biggs, I. W. A. Browne, P. Helbig, L. V. E. Koopmans, P. N. Wilkinson, R. A. Perley, MNRAS **304**, 349 (1999).

[9] B. F. Madore, *et al.* Astrophys. J. **515** 29 (1999).

[10] L. M. Krauss and M. S. Turner, Gen. Rel. Grav. **27**, 1137 (1995) [astro-ph/9504003].

[11] M. S. Turner and M. White, Phys. Rev. **D56**, 4439 (1997) [astro-ph/9701138].

[12] I. Zlatev, L. Wang and P. J. Steinhardt, Phys. Rev. Lett. **82**, 896 (1999) [astro-ph/9807002].

[13] M. S. Turner, G. Steigman and L. M. Krauss, Phys. Rev. Lett. **52**, 2090 (1984).

[14] S. Perlmutter *et al.* [Supernova Cosmology Project Collaboration], Nature **391**, 51 (1998) [astro-ph/9712212].

[15] A. G. Riess *et al.*, Astron. J. **116**, 1009 (1998) [astro-ph/9805201].

[16] S. Doddelson *et al.* Science **274**, 69 (1996).

[17] B. Chaboyer, P. Demarque, P. J. Kernan, L. M. Krauss, Science **271**, 957 (1996).

[18] K. Coble, S. Dodelson and J. A. Frieman, Phys. Rev. **D55**, 1851 (1997) [astro-ph/9608122].

[19] J. Peacock, MNRAS **284**, 885 (1997).

[20] P. J. Peebles and B. Ratra, Astrophys. J. **325**, L17 (1988).

[21] B. Ratra and A. Quillen, Mon. Not. Roy. Astron. Soc. **259**, 738 (1992).

[22] M. Birkel and S. Sarkar, Astropart. Phys. **6**, 197 (1997) [astro-ph/9605055].

[23] S. Podariu and B. Ratra, astro-ph/9910527.

[24] P. Steinhardt, in "Critical Problems in Physics," ed. by V. L. Fitch and D. R. Marlow (Princeton U. Press, 1997).

[25] R. R. Caldwell, R. Dave and P. J. Steinhardt, Phys. Rev. Lett. **80**, 1582 (1998) [astro-ph/9708069].

[26] P. G. Ferreira and M. Joyce, Phys. Rev. Lett. **79**, 4740 (1997) [astro-ph/9707286].

[27] C. Wetterich, Nucl. Phys. **B302**, 668 (1988).

[28] E. J. Copeland, A. R. Liddle and D. Wands, Phys. Rev. **D57**, 4686 (1998) [gr-qc/9711068].

[29] B. Ratra and P. J. Peebles, Phys. Rev. **D37** (1988) 3406.

[30] P. J. Steinhardt, L. Wang and I. Zlatev, Phys. Rev. **D59**, 123504 (1999) [astro-ph/9812313].

[31] T. Kajita [Super-Kamiokande Collaboration], Nucl. Phys. Proc. Suppl. **77**, 123 (1999) [hep-ex/9810001]; J. N. Bahcall, P. I. Krastev and A. Y. Smirnov, Phys. Lett. **B477**, 401 (2000) [hep-ph/9911248]; J. N. Bahcall, P. I. Krastev and A. Y. Smirnov, Phys. Rev. **D58**, 096016 (1998) [hep-ph/9807216].

[32] J. N. Bahcall, P. I. Krastev and A. Y. Smirnov, Phys. Lett. **B477**, 401 (2000) [hep-ph/9911248].

[33] A. de la Macorra, astro-ph/9911079.

[34] A. Singh, Phys. Rev. D **52**, 6700 (1995).

[35] M. Gell-Mann, *et al.*, in *Supergravity*, Proceedings of the Workshop, Stony Brook, New York, 1979, ed. P. van Nieuwenhuizen and D. Freedman, (North Holland, Amsterdam, 1979).

[36] L. M. Widrow, Phys. Rev. **D40**, 1002 (1989).

[37] R. N. Mohapatra and M. K. Parida, Phys. Rev. **D47**, 264 (1993).

[38] N. G. Deshpande, E. Keith, and P. B. Pal, Phys. Rev. **D46**, 2261 (1992).

[39] E. W. Kolb and M. S. Turner, *The Early Universe*, 73 (Addison-Wesley, Reading, MA, 1990).

[40] G. Huey, L. Wang, R. Dave, R. R. Caldwell, P. J. Steinhardt, astro-ph/9804285 (1998).

[41] J. A. Peacock and S. J. Dodds, MNRAS **267**, 1020 (1994).

[42] P. J. Steinhardt, *conversation and personal correspondence.*

[43] J. Schwinger, Proc. Nat. Acad. Sci. **91**, 6473 (1994); *ibid.* **90**, 7285 (1993); *ibid.* **90**, 4505 (1993); *ibid.* **90**, 2105 (1993); *ibid.* **90**, 958 (1993); *ibid.* **89**, 11118 (1992); and *ibid.* **89**, 4091 (1992).

[44] S. Liberati, M. Visser, F. Belgiorno, and D. W. Sciama, Phys. Rev. Lett. **83**, 678 (1999).

[45] S. Liberati, M. Visser, F. Belgiorno, and D. W. Sciama, quant-ph/9805031; quant-ph/9904013; quant-ph/9904018; and quant-ph/9905034.

[46] I. Brevik, V. N. Marachevsky, K. A. Milton, Phys. Rev. Lett. **82**, 3948 (1999); K. A. Milton and Y. Jack Ng, Phys. Rev. **E57** 5504 (1998); *ibid.* **E55**, 4207 (1997); K. Milton, *Casimir energy for a spherical cavity in a dielectric: toward a model for Sonoluminescence?*, in *Quantum field theory under the influence of external conditions*, edited by M. Bordag, (Tuebner Verlagsgesellschaft, Stuttgart, 1996), pages 13–23.

[47] C. E. Carlson, C. Molina-París, J. Pérez-Mercader, Matt Visser, Phys. Lett. **B395**, 76 (1997); Phys. Rev. **D56**, 1262 (1997).

[48] C. E. Carlson, T. Goldman, and J. Pérez-Mercader, Europhys. Lett. **36**, 637 (1996).

[49] S. Kulkarni *et al.*, Nature **393**, 35 (1998).

[50] See e.g., C. Kouveliotou, Ap. J. Supp. **92**, 637 (1994).

[51] S. Narayan, B, Pacziński, and T. Piran, Ap. J. **395**, L83 (1992).

[52] E. J. Schneid *et al.*, A. & A. **255**, L13 (1992); K. Hurley *et al.*, Nature **372**, 652 (1994).

[53] C. Molina-París and M. Visser, Phys. Rev. **D56** 6629 (1997).

[54] M. Ruffert and H.-Th. Janka, astro-ph/9804132 and astro-ph/9809280; H.-Th. Janka, Th. Eberl, M. Ruffert, and C. L. Fryer, astro-ph/9908290.

[55] J. Gorosabel, A. J. Castro-Tirado, S. Brandt, and N. Lund, Astronomy and Astrophysics **336**, 57 (1998); A. Singh and M. Srednicki, Ap. J. **492**, L29 (1998); R. Narayan and T. Piran, Mon. Not. Roy. Astron. Soc. **265**, L65 (1993).